Supplement of Atmos. Meas. Tech., 18, 3569–3584, 2025
https://doi.org/10.5194/amt-18-3569-2025-supplement

Supplement of

Improving consistency in methane emission quantification from the natural gas distribution systems across measurement devices

Judith Tettenborn et al.

Correspondence to: Thomas Röckmann (t.roeckmann@uu.nl)

Contents

S1 Instrument Characteristics

The G2301 instrument provides atmospheric mole fraction measurements of CH_4 with a data frequency of ≈ 0.36 Hz (every 2.8 s) with a precision of < 0.5 ppb within the operating range of 0-20 ppm.

The G2301-m greenhouse gas analyzer deploys cavity ring-down spectroscopy. It is a modification of the G2301 model designed to minimize effects induced by mobile measurements. It has an acquisition rate of 1 Hz and a precision of <1.5 ppb for CH_4.

The G2401 analyzer has a precision of < 1 ppb for CH_4 over a 5 s integration period.

The G4302 instrument has two operating modes. The one used was the 'ethane/methane' mode, which is characterized by a measurement frequency of > 1 Hz, a precision of 30 ppb in the operating range of 1-5000 ppm. Both instruments utilize cavity ring-down spectroscopy (CRDS) to measure CH_4.

The LI-7810 $CH_4/CO_2/H_2O$ Trace Gas Analyzer is a laser-based gas analyzer that uses Optical Feedback — Cavity-Enhanced Absorption Spectroscopy (OF-CEAS) to detect gases in air. It can measure CH_4 within the range 0-100 ppm with a precision (1 σ) of 0.6 (0.25) ppb at 2 ppm with 1 (5) s averaging. Its response time $(\mathrm{T}_{10} - \mathrm{T}_{90}$ from 0 to 2 ppm is $\leq 2\ \mathrm{s}$.

The MGA10 analyzer measured at 1 Hz with precision of 1 ppb within the measurement range 0-200 ppm.

The Mira Ultra instrument has a measurement frequency of 1 Hz, a sensitivity of $< 2\ \mathrm{ppbs}^{-1}$ and an operation range 0.02-10,000 ppm. The temporal response is 1 s and it takes 3 s to 90 $\%$ recovery with it's internal pump. It deploys a mid-infrared laser absorption spectroscopy technology.

The TILDAS Dual Laser Trace Gas Analyzer measured at 1 Hz with precision of 2.4 ppb and had a response time equal to about 2 s.

The UGGA device has a precision of $< 2\ \mathrm{ppb}$ for CH_4 over a 1 s integration period and its measurement range lies between 0.01-100 ppm.

The uMEA analyzer uses laser absorption spectroscopy, delivering linear measurements within the range 0.01-100 ppm and has a precision of 3 ppb for CH_4 over a one second period.

The control range of the Alicat mass flow controller is 0-100 Lmin^{-1} under standard conditions with a measurement accuracy of ±(0.8% of reading + 0.2% of full scale).

The residence time within the measurement cell for the different instruments was determined on the basis of the cell temperature T_{cell} $[\mathrm{K}]$, cell pressure p_{cell} $[\mathrm{Pa}]$, cell volume V_{cell} $\left[\mathrm{m}^3\right]$ and flow rate Q_{cell} $[\mathrm{slm}]$ specified by the manufacturers (given in Tab. S1). The units in brackets specify the units in which the different quantities have to be inserted into the equations Eq. S1 and Eq. S2.

The normalized volume (scaled to standard pressure 101325 Pa and standard temperature 25°C) was calculated:

$$V_{\mathrm{norm}} = \frac{p_{\mathrm{cell}} \cdot V_{\mathrm{cell}} \cdot R \cdot T_{\mathrm{norm}}}{R \cdot T_{\mathrm{cell}} \cdot p_{\mathrm{norm}}} \tag{S1}$$

Then, given the flow rate, the residence time was determined from V_{norm} and the flow rate Q_{cell} as:

$$\tau = \frac{V_{\mathrm{norm}}}{Q_{\mathrm{cell}}} \tag{S2}$$

Table S1. Overview of instrument characteristics of analyzers deployed in the controlled release experiments. In cases where flow rate varied, the bold numbers were used for the calculation of the residence time. The integration time over which the precision applies was not available for some instruments.

GHG Analyzer	T_{cell} [°C]	p_{cell} [mbar]	V_{cell} [mL]	Air Volume in Cell $V_{\mathrm{norm}}(p,T)$ [mL]	Q_{cell} [slm]	τ [s]	Measurement Frequency [Hz]	Precision (Integration Periode) [ppb] ([s])
G2301[a]	45	190	50	8.8	0.4	1.3	0.36	<0.5
G2401[a]	35	186	35	6.0	0.4	0.9	0.4	<1 (5)
G4302[a]	35	600	35	21.8	2.4	0.5	1	30
LI-7810[b]	55	390	6.41	2.2	0.25	0.5	1	0.6 (1)
MGA10[c]	27	80	500	39.2	4	0.6	2	1
Mira Ultra[d]	42	240	60	13.5	0.3-**0.6**	1.3	1	0.6 (1)
TILDAS[e]	25	40	500	19.7	6	0.2	2	2.4
UGGA[f]	25	186	345	63.3	**2**-4	1.9	0.1-1	<2 (1)
uMEA[f]	.	.	.	345	.	.	1	3 (1)

[a] Picarro INC, Santa Clara, USA. [b] LI-COR Environmental, Lincoln, USA. [c] MIRO Analytical AG, Wallisellen, CH. [d] Aeris Technologies, Eden Landing Road Hayward, CA. [e] Aerodyne Research, Billerica, USA. [f] Los Gatos Research, San Jose, USA.

S2 Description Controlled Release Experiments

S2.1 Release Locations

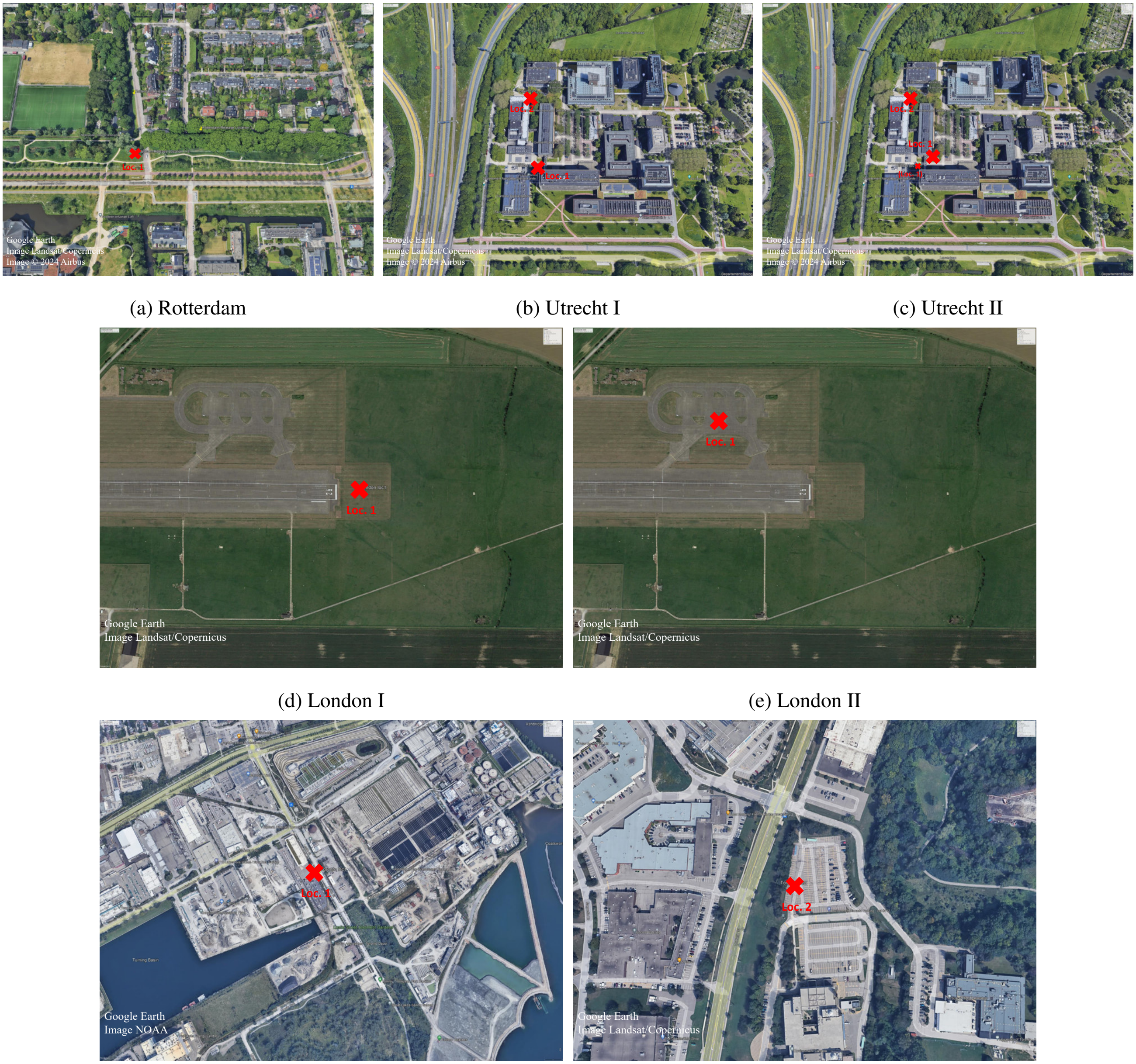

(a) Rotterdam

(b) Utrecht I

(c) Utrecht II

(d) London I

(e) London II

(f) Toronto Loc. 1

(g) Toronto Loc. 2

Figure S1. ©Google Earth screenshots of locations of the different controlled release experiments (©Google Earth, Image Landsat/Copernicus and Image ©2024 Airbus and Image NOAA). The red crosses indicate the location of the controlled CH_4 releases.

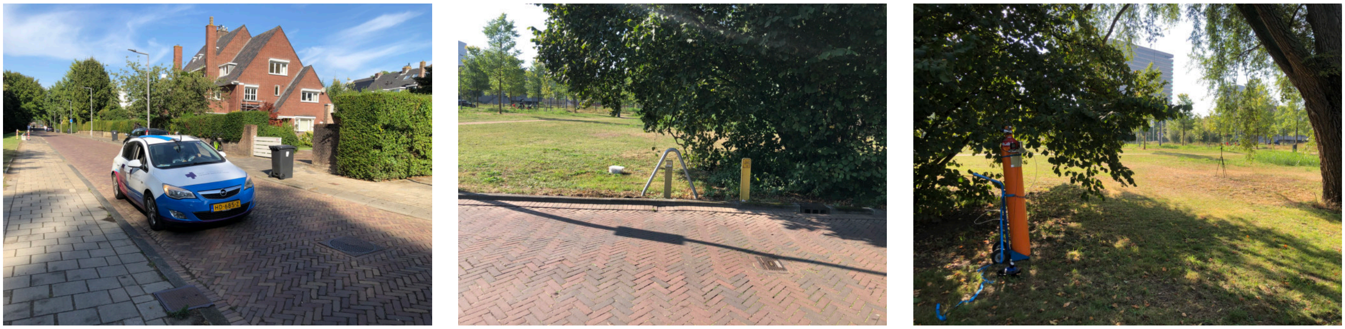

(a) UUAQ car

(b) Location 1 - release

(c) Location 1 - gas vessel

Figure S2. Rotterdam: Overview of measurement set-up.

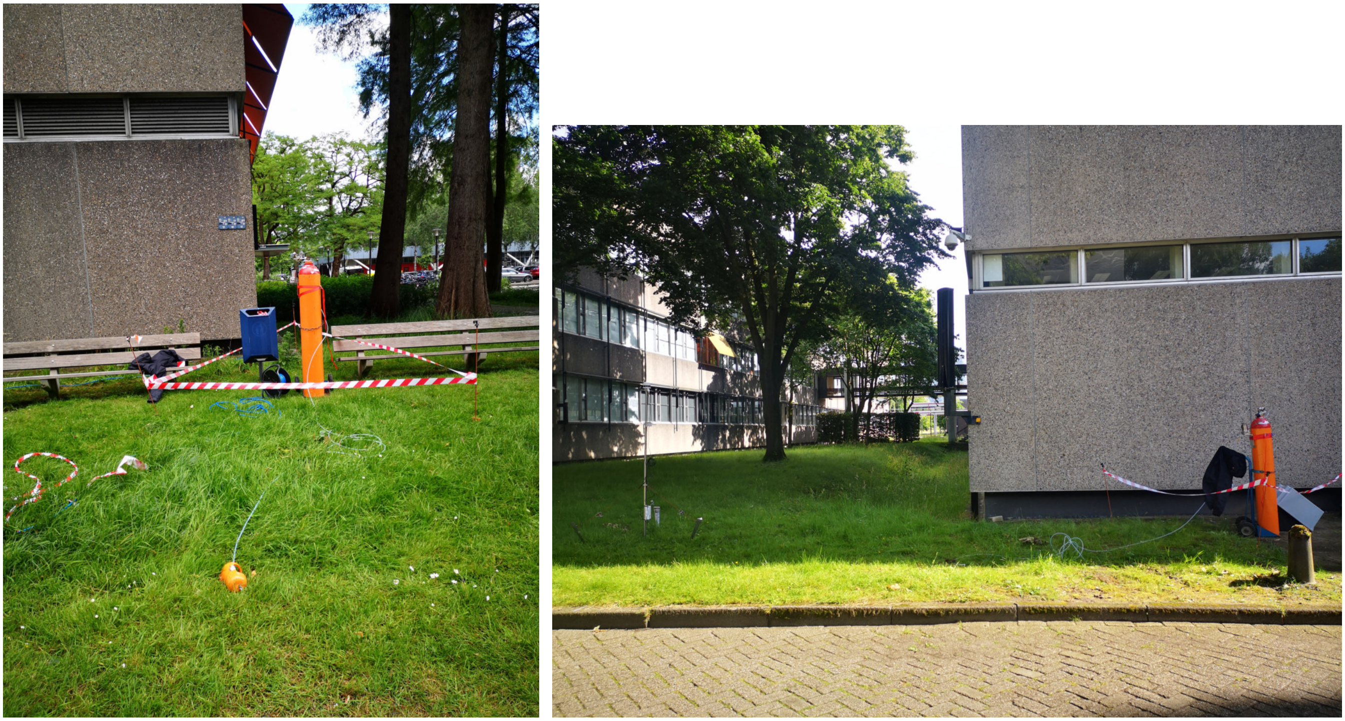

(a) Location 1

(b) Location 2

Figure S3. Utrecht II: Overview of measurement set-up.

S2.2 Release Rates, Detection Counts, and Timing Overview

Table S2: Controlled Release Experiments: Overview of release rates, duration of releases per location, number of valid transects, and number of valid peaks. In cases where several instruments were mounted on the same vehicle, the number of peaks is higher than the number of transects. The time is given as local time (difference to UTC: London I UTC+01:00, London II UTC+01:00, Rotterdam UTC+02:00, Toronto UTC+04:00, Utrecht I UTC+01:00, Utrecht II UTC+02:00,). The number of transects/peaks with bike and car platforms is given separately for Toronto Day1 (bike + car).

City	Location	Release Rate $\left[\mathrm{L\,min^{-1}}\right]$	Duration (local time)	Valid Transects	Valid Peaks
London I Day1 (September 10, 2019)					
	1	70	11:01 - 15:42	36	72
	1	35	16:01 - 17:20	13	26
London I Day2 (September 11, 2019)					
	1	35	12:16 - 13:05	15	30
	1	70	13:22 - 14:11	10	20
	1	70	16:28 - 17:20	22	44
London I Day3 (September 13, 2019)					
	1	70	10:25 - 11:53	42	42
London II Day1 (May 13, 2024)					
	1	70.5	14:18 - 14:44	31	31
	1	50.5	15:03 - 15:31	29	29
	1	30.6	15:38 - 15:58	29	29
	1	10.6	16:14 - 16:40	24	24
	1	5.6	16:44 - 17:06	26	26
	1	1	17:14 - 17:36	22	22
	1	30.6	17:47 - 18:15	49	49
London II Day2 (May 14, 2024)					
	1	1	10:08 - 10:47	40	40
	1	0.5	11:02 - 11:32	34	34
	1	0.2	11:37 - 12:23	1	1
Rotterdam (September 6, 2022)					
	1	5	9:05 - 10:15	49	138

Continued on next page

Table S2 – continued from the previous page

City	Location	Release Rate $\left[\mathrm{L\,min^{-1}}\right]$	Duration (local time)	Valid Transects	Valid Peaks
	1	10	10:15 - 10:58	35	97
	1	20	10:58 - 11:23	21	61
	1	40	11:23 - 11:54	34	97
	1	80	11:54 - 12:44	44	124
	1	20	13:05 - 13:34	6	24
	1	120	13:34 - 13:48	3	12
	1	40	13:48 - 14:26	6	24
	2	1	10:28 - 11:01	21	62
	2	0.15	11:01 - 11:39	20	59
	2	0.515	11:39 - 12:12	23	66
	2	0.31	12:12 - 13:16	22	66
	3	3.33	13:16 - 14:26	9	36
Toronto Day1 (October 20, 2021)					
	1	9.9	16:11 - 16:18	4+4	4+4
	1	5	16:19 - 16:27	5+4	5+4
	1	2.5	16:30 - 16:40	5+7	5+7
	1	19.8	16:40 - 16:49	5+5	5+5
Toronto Day2 (October 24, 2021)					
	2	9.9	9:48 - 9:58	7	7
	2	5	10:03 - 10:11	7	7
	2	1	10:16 - 10:24	11	11
	2	0.12	10:28 - 10:37	4	4
	2	0.5	10:41 - 10:59	19	19
Utrecht I (November 25, 2022)					
	1	3	13:06 - 13:46	24	48
	1	2.18	14:22 - 15:17	28	56
	2	15	13:06 - 13:46	61	122
	2	15	14:22 - 15:17		

Continued on next page

Table S2 – continued from the previous page

City	Location	Release Rate $\left[\mathrm{L\,min^{-1}}\right]$	Duration (local time)	Valid Transects	Valid Peaks
Utrecht II (June 11, 2024)					
	1	4	10:48 - 11:22	10	10
	1	4	11:38 - 11:48	5	5
	1	10	11:48 - 12:18	6	6
	1	80	12:18 - 12:32	6	11
	1	20	12:32 - 13:01	23	46
	1	100	14:05 - 14:21	10	20
	1	15	14:28 - 15:23	32	64
	1	4	16:19 - 17:07	18	35
	1	0.15	17:07 - 17:44	2	2
	1	1	17:44 - 17:56	1	1
	2	2.5	10:50 - 11:31	16	16
	2	4	11:31 - 12:09	12	12
	2	0.5	12:09 - 12:37	13	20
	2	0.15	12:37 - 13:01	10	20
	2	0.3	14:02 - 14:40	5	10
	2	2.2	14:40 - 15:13	18	36
	2	1	15:13 - 15:52	19	38
	2	4	17:00 - 17:30	17	22
	2	60	17:30 - 17:38	3	3
	2	20	17:38 - 18:06	11	11
	2	80	18:06 - 18:25	16	32

S3 Raw Data Processing

The raw measurements taken by the G4302, G2301 and Mira Ultra instruments during the Rotterdam, Utrecht I and Utrecht II controlled releases were corrected utilising calibration equations obtained by calibration measurements in the IMAU laboratory. The data collected by the other CH_4 analyzer were treated and calibrated by the team that deployed them.

G2301:

$$[\mathrm{CH_4}]_{\mathrm{calibrated}} = 1.03127068196 \cdot [\mathrm{CH_4}]_{\mathrm{raw}} - 0.15799666857 \tag{S3}$$

G4302:

$$[\mathrm{CH_4}]_{\mathrm{calibrated}} = 1.01924906721 \cdot [\mathrm{CH_4}]_{\mathrm{raw}} - 0.05887406866 \tag{S4}$$

Mira Ultra:

$$[\mathrm{CH_4}]_{\mathrm{calibrated}} = 1.01354227768 \cdot [\mathrm{CH_4}]_{\mathrm{raw}} - 0.05055326961 \tag{S5}$$

$[\mathrm{CH_4}]$ refers to the CH_4 mole fraction in ppm.

S4 Overview Time Series

Fig. S4 to Fig. S9 show an overview of selected timeseries. The different release rates translate into different peak heights over time. The methane mole fractions measured by different instruments differ strongly, even though the instruments transect the CH_4 plume simultaneously and draw air from the same inlet.

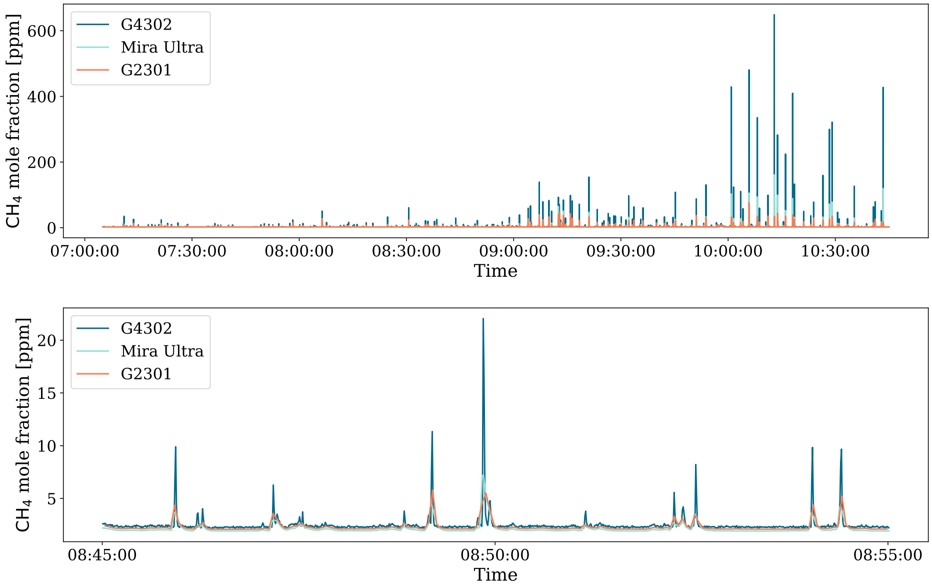

Figure S4. Rotterdam: Timeseries of CH_4 mole fraction, obtained by the G4302, G2301 and Mira Ultra devices, while installed in the UUAQ car. The lower panel displays a zoom to a 10 min measurement interval. Time displayed in UTC.

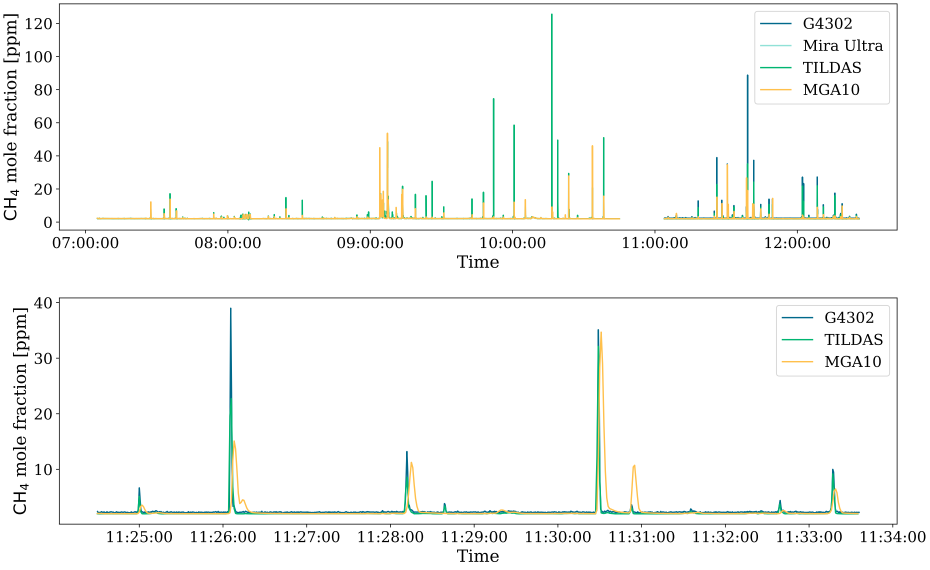

Figure S5. Rotterdam: Timeseries of CH$_4$ measurements, obtained by the MGA10, TILDAS, G4302 and Mira Ultra devices, while installed in the TNO truck. The lower panel displays a zoom to a 10 minutes measurement interval. Time displayed in UTC.

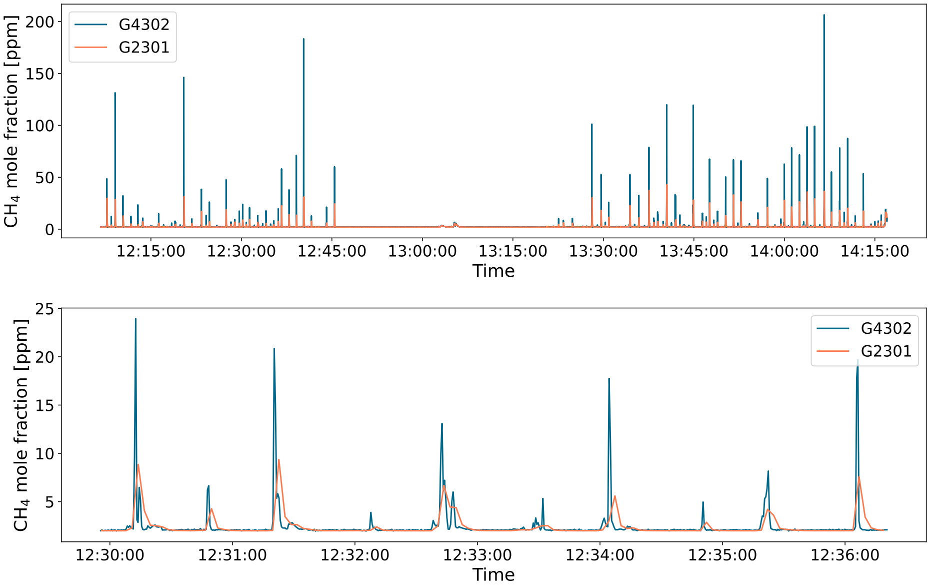

Figure S6. Utrecht I: Timeseries of CH$_4$ measurements, obtained by the G4302 and G2301 devices. The lower panel displays a zoom to a 6 minutes measurement interval. Time displayed in UTC.

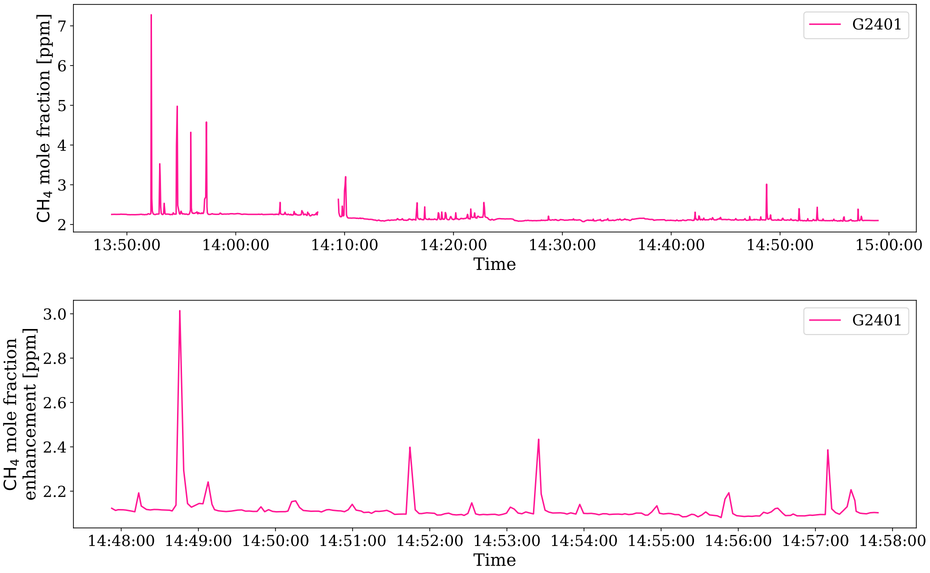

Figure S7. Toronto Day 2 - car: Timeseries of CH$_4$ measurements, obtained by the G2401 device. The lower panel displays a zoom to a 10 minutes measurement interval. Time displayed in UTC.

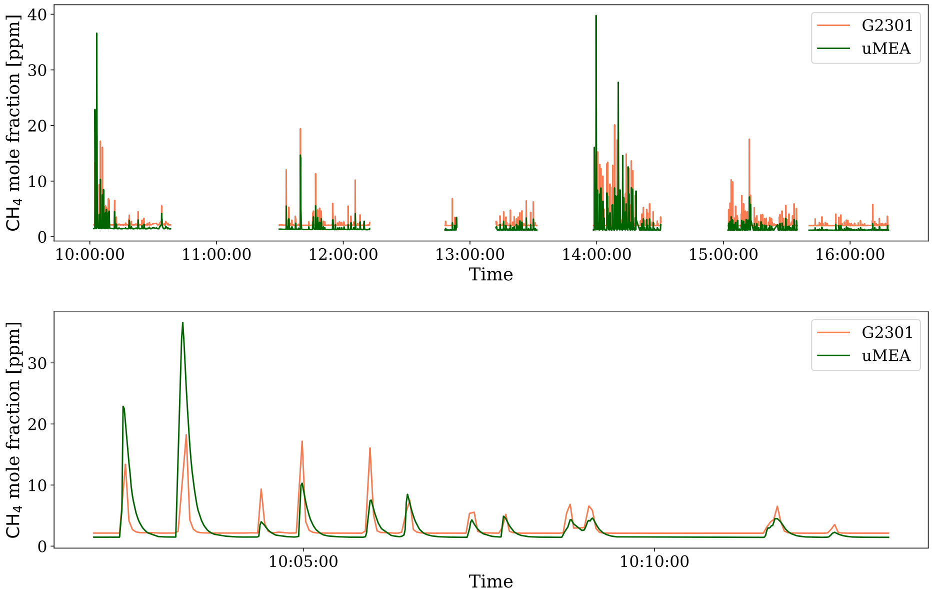

Figure S8. London I Day 1: Timeseries of CH$_4$ measurements, obtained by the G2301 and uMEA devices. The lower panel displays a zoom to a 10 minutes measurement interval. Time displayed in UTC.

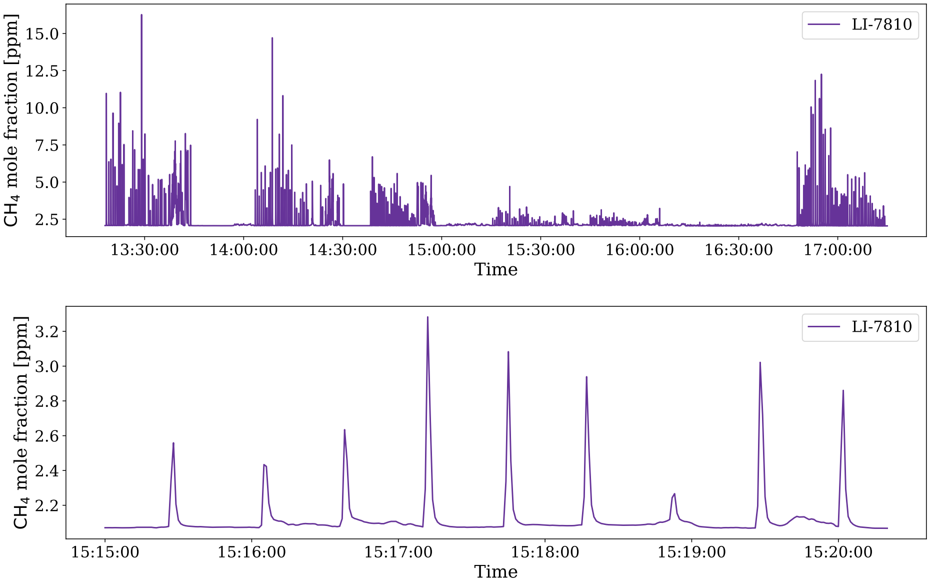

Figure S9. London II Day 1: Timeseries of CH_4 measurements, obtained by the LI-7810 device. The lower panel displays a zoom to a 5 minutes measurement interval. Time displayed in UTC.

S5 Background Comparison

Different background mole fraction definitions are used in the literature, using either a fixed threshold or a dynamic one, which offer the advantage to take temporal or spatial variability in the background level into account (von Fischer et al., 2017). Commonly, a moving window is applied and the background is defined as a specific percentile of the data range. Different percentiles were used in the previous literature to set the background, ranging from the 5^{th} percentile in Ars et al. (2020) to the 50^{th} percentile (median) in Weller et al. (2018) or taking the mean in von Fischer et al. (2017). Higher percentiles will be more strongly influenced by high CH_4 mole fractions when transecting a plume. The mean will be even more distorted towards higher values than the median. This can lead to high background mole fractions which do not represent the ambient background, but are artefacts of a spatially extended CH_4 plume. In this study, the background was defined as the 10^{th} percentile of the CH_4 mole fractions, which was assessed to represent the background well (Fig. S10). The 50^{th} percentile was too strongly influenced by the CH_4 release, occasionally showing up to $0.3\ \mathrm{ppm}$ higher background mole fractions compared to the 10^{th} percentile.

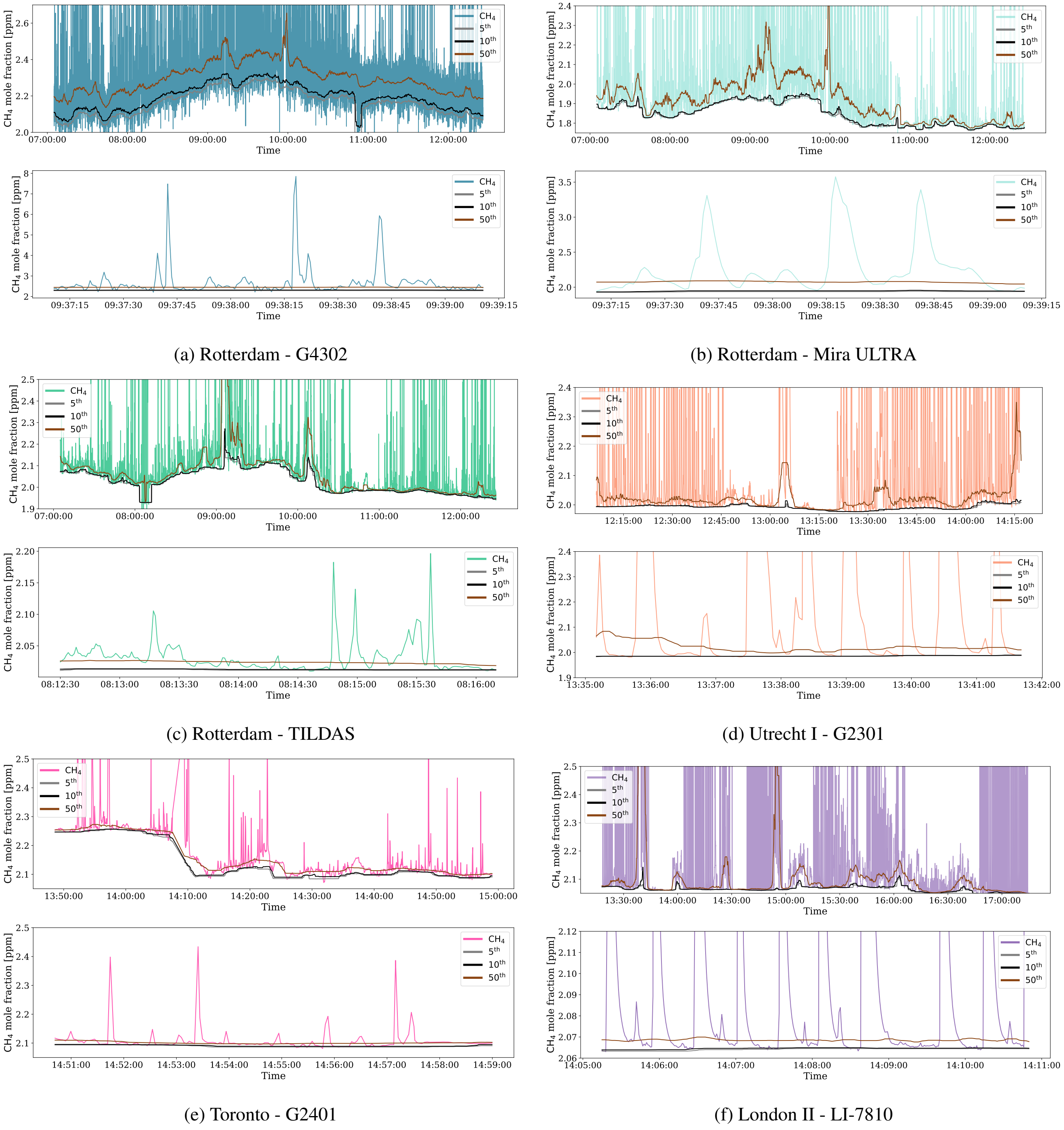

(a) Rotterdam - G4302

(b) Rotterdam - Mira ULTRA

(c) Rotterdam - TILDAS

(d) Utrecht I - G2301

(e) Toronto - G2401

(f) London II - LI-7810

Figure S10. Comparison of different background concentrations, determined using three different threshold levels (5$^{\text{th}}$, 10$^{\text{th}}$ and 50$^{\text{th}}$ percentile). The y-axis is truncated to enhance readability.

S6 Distance Analysis

The left panel in Fig. S11 visualizes the logarithm of the spatial peak area measured per transects from all controlled release experiments as function of the distance to the CH_4 release location. The right panel of Fig. S11, along with both panels in Fig. S12–Fig. S14 presents the same relationship separately for the different controlled release experiments, with the various release rates distinguished by colour. To evaluate the nature of this relationship, a linear regression was fitted to the log spatial peak area and distance values for each release rate. The spatial peak area values generally decrease with increasing distance, though the effect varies across cases and is relatively minor in most cases within a 75 m range. At some instances, e.g. for the 5 Lmin^{-1} release in Rotterdam, the linear regression fit even shows a positive slope, suggesting an increase in spatial peak area values with distance. This could be due to the small sample size and the strong influence of noise, such as changing winds or turbulence. For example, if turbulent motions cause the plume to diffuse more strongly (both horizontally and vertically) at a given moment, a transect passing nearby may measure a smaller spatial peak area than a more distant transect, where the wind conditions allowed the plume to remain relatively compact with minimal diffusion. Overall, these findings suggest that distance may not be a major factor affecting peak detection in urban areas, where peaks are expected to be identified primarily within a 75 m range from the source.

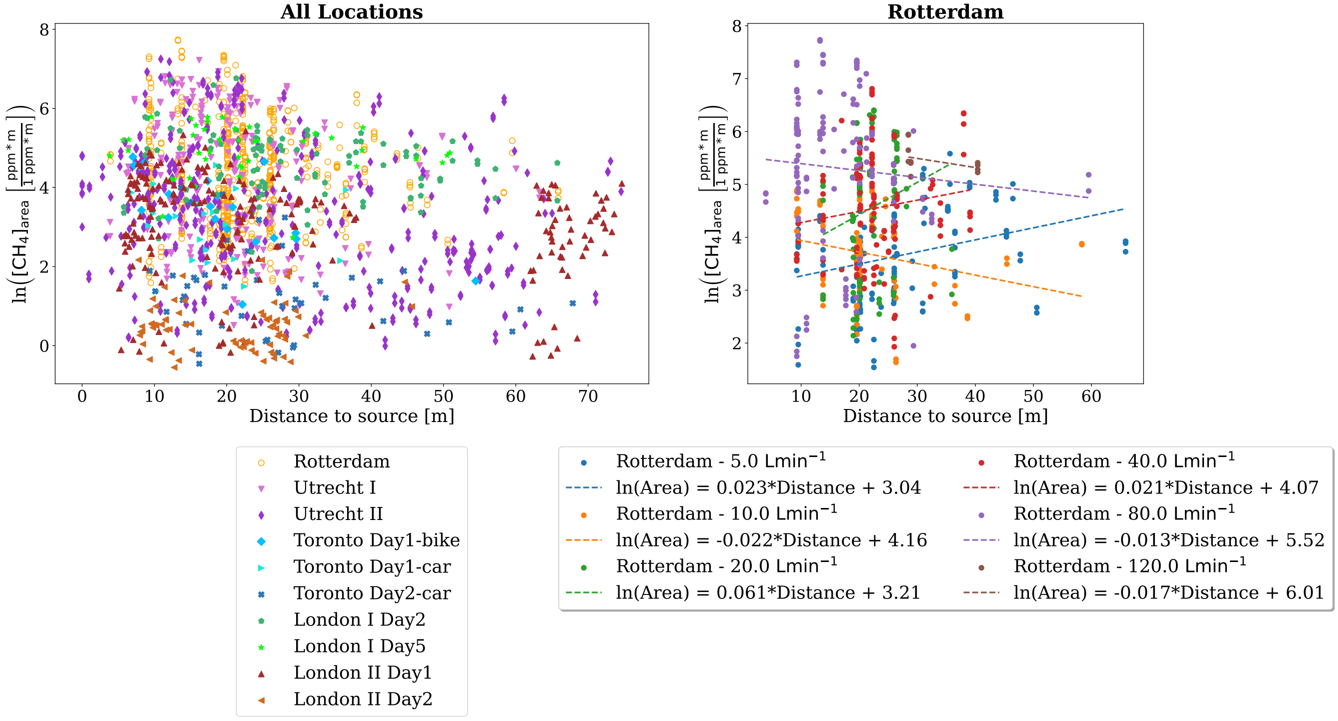

Figure S11. Logarithmic spatial peak area as function of distance to source for all individual CH_4 enhancements reported in this study (a) and Rotterdam (b). In panel (b), colours represent different release rates, with a separate linear regression fitted for each rate.

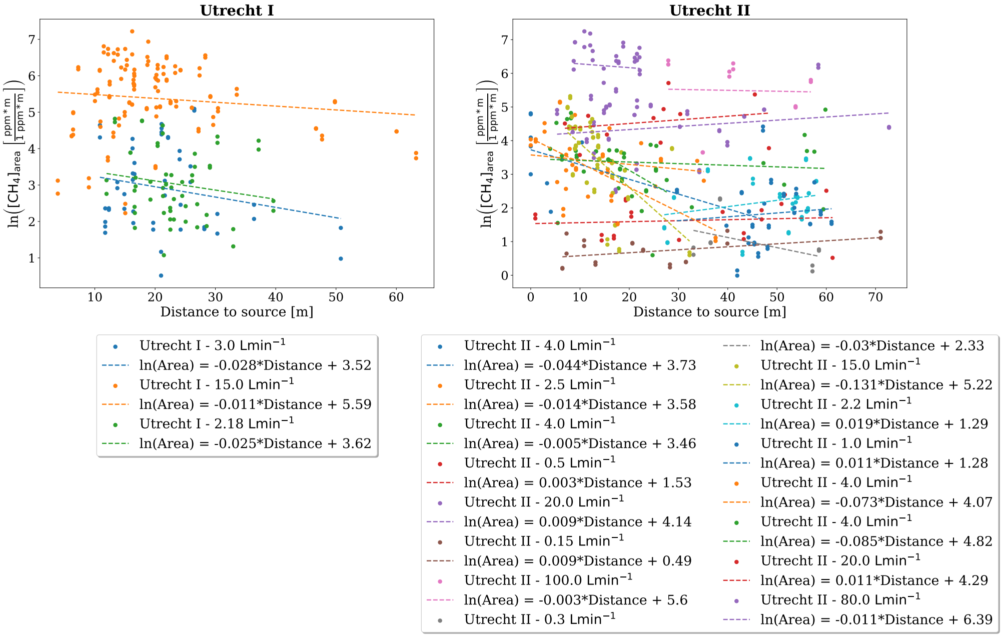

Figure S12. Logarithmic spatial peak area as function of distance to source for individual CH_4 enhancements reported in the Utrecht I (a) and Utrecht II (b) controlled release experiment. Colours represent different release rates, with a separate linear regression fitted for each rate.

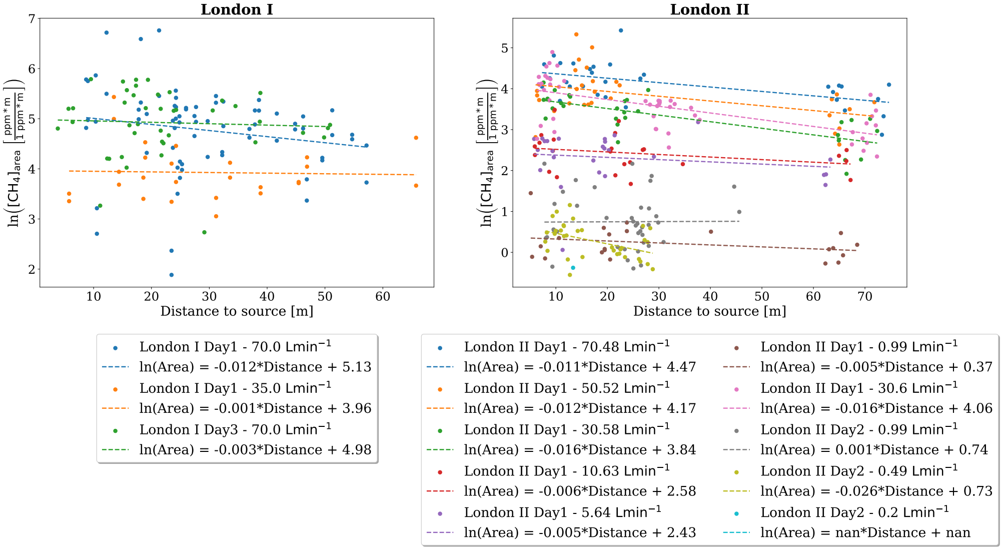

Figure S13. Logarithmic spatial peak area as function of distance to source for individual CH_4 enhancements reported in the London I (a) and London II (b) controlled release experiment. Colours represent different release rates, with a separate linear regression fitted for each rate.

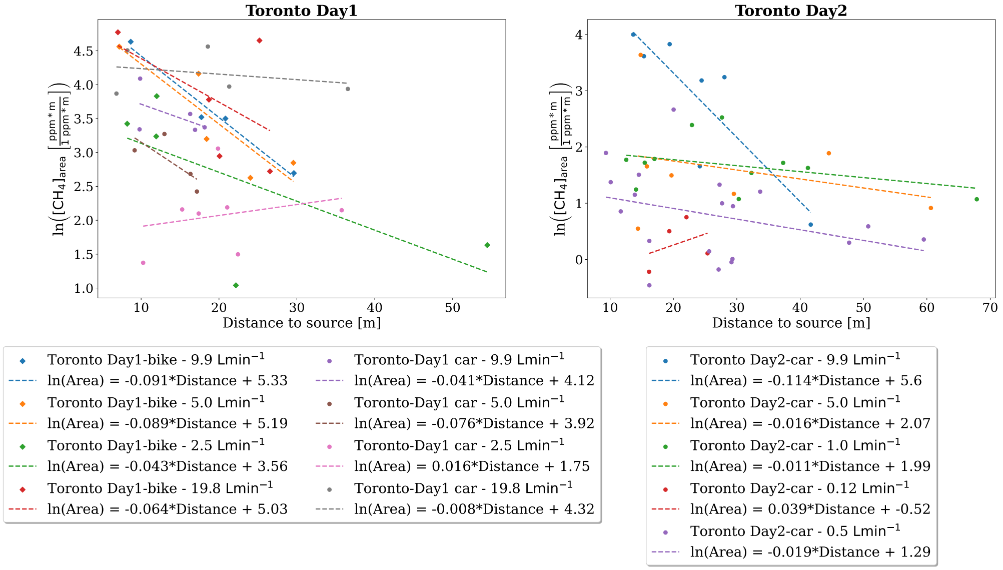

Figure S14. Logarithmic spatial peak area as function of distance to source for individual CH_4 enhancements reported in the (a) Toronto Day1 and (b) Day2 controlled release experiment. Colours represent different release rates, with a separate linear regression fitted for each rate.

S7 Model Diagnostics

There are four main assumptions underlying a linear regression model which describes the relation of a response variable Y and a predictor variable X (Von Storch and Zwiers, 2002; Flatt and Jacobs, 2019):

1. Linearity: The relationship between X and the mean of Y is linear.
2. Homoscedasticity: The variance of residuals is the same for any value of X.
3. Independence: Observations are independent of each other.
4. Normality: For any fixed value of X, the error terms (residuals) of Y are normally distributed.

Violations of these assumptions can lead to biased and misleading inferences, confidence intervals, and scientific insights (Flatt and Jacobs, 2019).

S7.1 Analysis of Residuals

To judge on linearity, it can be helpful to visualize the shape of the residuals. This can be done via a standardized residuals plot, where systematic behaviour can be assessed (Von Storch and Zwiers, 2002; Biecek and Burzykowski, 2021). Standardized residuals are the differences between the observed values and the values predicted by the fitted linear regression model, divided by the standard deviation of the error estimates:

$$\frac{\ln([\mathrm{CH_4}]_{\mathrm{area}})^{\mathrm{measured}} - \ln([\mathrm{CH_4}]_{\mathrm{area}})^{\mathrm{predicted}}}{\sigma} \tag{S6}$$

They are plotted against the estimated conditional mean $\mu_{\mathbf{Y}_i|\mathbf{X}=\mathbf{x}_i}$, i.e. the values predicted by the regression (in this case $\ln([\mathrm{CH_4}]_{\mathrm{area}})$) for the given values of the independent variable ($\ln(\mathrm{r_E})$). Homoscedasticity means errors e_i all have common variance. Violations of this can influence the coefficients derived under ordinary least-squares regression. Scatter plots of the absolute residuals can help detecting heteroscedasticity. The third assumption necessitates observations to be independent of each other. Paired samples represent the most basic example of non-independent data. When data fail to satisfy the independence assumption, it can impair the accuracy of test statistics (Nimon, 2012). In a good fitting model, residuals should exhibit random, not systematic deviations from zero. This entails their distribution being symmetric around zero (mean should be zero). Additionally, residuals should have minimal variability, ideally being close to zero themselves (Biecek and Burzykowski, 2021). Normality can be assessed using quantile-quantile plots (QQ plot) or test statistics, whereby the Shapiro-Wilk test was found to be the most powerful tests in most situations (Keskin, 2006; Razali and Wah, 2011). Here, the Shapiro-Wilk and the Lilliefors test (a modification of the Kolmogorov-Smirnov test) were applied to the residuals, using a 5% significance level. This was done utilizing the *scipy.stats module* (*stats.shapiro*) and the *statsmodels.stats.diagnostic* module (*lilliefors*).

Fig. S15 illustrates the standardized residuals for the area linear regression model. The x-axis displays the predicted values of $\ln([\mathrm{CH_4}]_{\mathrm{area}})^{\mathrm{predicted}}$), i.e. the vertical point clouds represent the different release rates, but plotted here in terms of the corresponding $\ln([\mathrm{CH_4}]_{\mathrm{area}})$ estimate based on the Area eq. For visibility, the different releases were plotted in two groups and only distribution with at least 10 observations are shown.

The majority of the means (indicated as a black dot) fall relatively close to the zero line. There is a small tendency towards negative deviations from zero for the means. The residuals do not scatter symmetrically around their mean for all distributions. Clustering of data towards the center can be indicative of a normal distribution. This seems to be the case e.g. for the release rate 40 $\mathrm{Lmin^{-1}}$ (Fig. S15b, $\ln([\mathrm{CH_4}]_{\mathrm{area}}) = 4.7$), where also the mean is close to zero. However, other distributions of residuals are more scattered. Some distributions show long tails, suggesting skewness in the distribution, e.g. residuals at 15 $\mathrm{Lmin^{-1}}$ in Utrecht I or 80 $\mathrm{Lmin^{-1}}$ in Rotterdam (Fig. S15b, corresponding to an $\ln([\mathrm{CH_4}]_{\mathrm{area}})$ estimate of 3.9 and 5.2 respectively).

The absolute standardized residuals predominantly remain below 3, and mostly even under 2. There is a weak trend of increasing residual variability with higher release rates. Nonetheless, this trend is marked by significant fluctuations (Fig. S15b, lower panels).

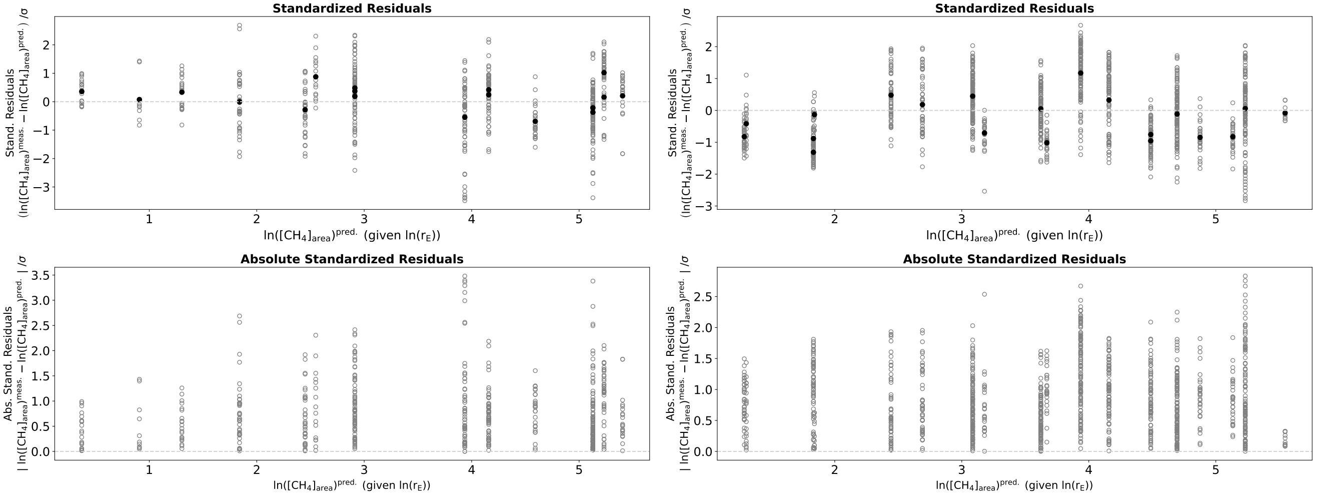

(a) Utrecht II and London I

(b) Rotterdam, Utrecht I, London II, Toronto

Figure S15. Standardized residuals (differences between the measured values and the values predicted by the fitted line, divided by the standard deviation of the error estimates) plotted against the conditional estimate $\ln([\mathrm{CH_4}]_{\mathrm{area}})_i^{\mathrm{pred.}} \mid X = \ln(\mathrm{r_E})_i$ for the linear regression (upper panel). The lower panel displays the absolute values of these standardized residuals. For better visibility, the dataset was separated into (a) Utrecht II and London I and (b) Rotterdam, Utrecht I, London II, Toronto data.

S7.2 Statistical Normality Tests

The results (pass or fail, p-values and statistics) of the Shapiro-Wilk (SW) and the Lilliefors test are provided in Tab. S3 to Tab. S7. Data with small sample size were omitted from this analysis.

From the 6 assessed release rates for Rotterdam, 4 passed the Shapiro-Wilk test and even 3 passed the Lilliefors test, which means the hypothesis that the data follow a normal distribution could not be rejected in those cases (Tab. S3). It was rejected however in both tests for the release rate of 20 Lmin^{-1} and 80 Lmin^{-1}. Despite having high test statistics for the SW test, the corresponding p-values are low. Only the 2.18 Lmin^{-1} release in Utrecht I passed both tests (Tab. S4). The p-value for the 3 Lmin^{-1} release, which passes the SW test, is 0.039 for the Lilliefors test, so comparably close to 0.05, therefore only narrowly failing. In Utrecht II 6 of the 10 distributions pass the SW test and 6 the Lilliefors test (Tab. S5). For the London CREs, two out of three experiments pass the Lilliefors normality test, while only one out of three passes the Shapiro-Wilk test (Tab. S6). For a release rate of 35 Lmin^{-1}, both tests indicate normality. For the 70 Lmin^{-1} release rate, the outcomes differ between the two tests and experiment days. In London II 7 of the 9 releases pass the SW test, while all pass the Lilliefors test (Tab. S7).

Overall, in most cases half or the majority of distributions passes the normality tests. This means on the other side that a significant number of distributions do not pass. The statistic values from the Lilliefors test are generally lower compared to the Shapiro-Wilk test, which may suggest that the Lilliefors test is less sensitive to deviations from normality in these specific datasets.

Table S3. Rotterdam: Normality statistics summary.

Release Rate	Dataset Size	Shapiro-Wilk Test			Lilliefors Test		
[Lmin^{-1}]		Result	p-value	Statistic	Result	p-value	Statistic
5	138	pass	0.367	0.989	pass	0.707	0.047
10	97	pass	0.547	0.988	pass	0.441	0.064
20	85	fail	0.0	0.918	fail	0.002	0.133
40	121	pass	0.782	0.993	pass	0.730	0.049
80	124	fail	0.0	0.956	fail	0.017	0.093
120	12	pass	0.057	0.865	fail	0.016	0.273

Table S4. Utrecht I: Normality statistics summary.

Release Rate	Dataset Size	Shapiro-Wilk Test			Lilliefors Test		
[Lmin^{-1}]		Result	p-value	Statistic	Result	p-value	Statistic
2.18	56	pass	0.168	0.97	pass	0.613	0.076
3	48	pass	0.078	0.957	fail	0.039	0.132
15	122	fail	0.0	0.950	pass	0.073	0.08

Table S5. Utrecht II: Normality statistics summary.

Release Rate	Dataset Size	Shapiro-Wilk Test			Lilliefors Test		
[Lmin^{-1}]		Result	p-value	Statistic	Result	p-value	Statistic
0.15	29	fail	0.002	0.865	pass	0.198	0.135
0.5	20	pass	0.412	0.953	pass	0.246	0.153
1	39	pass	0.246	0.964	pass	0.690	0.084
2.2	36	pass	0.385	0.968	pass	0.628	0.091
2.5	16	pass	0.879	0.973	pass	0.85	0.111
4	79	pass	0.116	0.975	pass	0.07	0.1
15	70	fail	0.0	0.926	fail	0.001	0.152
20	67	pass	0.067	0.966	fail	0.039	0.116
80	46	fail	0.003	0.918	fail	0.008	0.155
100	28	fail	0.002	0.863	fail	0.001	0.222

Table S6. London I: Normality statistics summary.

Release Rate	Dataset Size	Shapiro-Wilk Test			Lilliefors Test		
[Lmin^{-1}]		Result	p-value	Statistic	Result	p-value	Statistic
35	60	pass	0.067	0.963	pass	0.117	0.106
70	114	fail	0.0	0.956	fail	0.017	0.096
70	42	fail	0.004	0.913	pass	0.147	0.119

Table S7. London II: Normality statistics summary.

Release Rate	Dataset Size	Shapiro-Wilk Test			Lilliefors Test		
[Lmin^{-1}]		Result	p-value	Statistic	Result	p-value	Statistic
0.49	34	pass	0.879	0.984	pass	0.751	0.087
0.99	40	pass	0.254	0.965	pass	0.461	0.096
0.99	22	fail	0.016	0.886	pass	0.107	0.168
5.64	26	fail	0.0	0.827	pass	0.129	0.152
10.63	24	pass	0.713	0.972	pass	0.679	0.106
30.58	30	pass	0.054	0.932	pass	0.174	0.136
30.6	51	pass	0.622	0.982	pass	0.749	0.071
50.52	29	pass	0.537	0.969	pass	0.463	0.112
70.48	31	pass	0.725	0.977	pass	0.286	0.122

S7.3 Spatial Peak Area distribution per Release Rate

Fig. S16 to Fig. S20 provide an overview of the spatial peak area distributions per release rate in the form of histograms and quantile-quantile (QQ) plots. For each histogram, a Gaussian distribution is plotted together with the data, employing mean and standard deviation derived from the underlying dataset. In the QQ plots, the vertical axis displays the ordered logarithmic spatial peak area values, while the horizontal axis displays expected values based on the standard normal distribution. When the normality assumption is met, the plot should exhibit points scattered closely along the 45-degree diagonal line. While the normality assumptions must be met by the residuals, here the $\ln([\mathrm{CH}_4]_{\mathrm{area}})$ values are plotted for easier comparison with Figure 3 in the main manuscript. Since the residuals for each release rate are obtained by subtracting a scalar from the $\ln([\mathrm{CH}_4]_{\mathrm{area}})$ distribution, the distribution's shape remains unchanged and is simply shifted by this scalar.

For Rotterdam the histograms for the 20, and 80 Lmin^{-1} releases appear to exhibit a bimodal shape (Fig. S16a). This is also reflected in the QQ plots of the 20 and 80 Lmin^{-1} release rates (Fig. S16b). Variations are observed in the central body of the 80 $\mathrm{Lmin^{-1}}$ release, and more pronounced deviations are evident in the case of the 20 $\mathrm{Lmin^{-1}}$ release, which exhibits an s-shaped pattern. This visualizes why the normality tests fail. For the other releases (except 120 $\mathrm{Lmin^{-1}}$, for which the low number of data points makes an analysis difficult) the distribution aligns well with the 1:1 line in the QQ plots. In all instances, the highest quantiles consistently appear below the $45°$ line, indicating a scarcity of data in the high range compared to a normal distribution (a thinner tail on the right side). For some cases, the points also fall below the 1:1 line for the lowest quantiles, implying a higher abundance of data at the low range compared to a normal distribution (a fatter tail on the left side).

Both the histogram and QQ plot of the 2.18 $\mathrm{Lmin^{-1}}$ release in Utrecht I confirm the positive assessments of both normality tests (Fig. S17). However, the 3 $\mathrm{Lmin^{-1}}$ QQ plot exhibit an s-shaped form, confirming the fat tails visible in the histogram plot. The 15 $\mathrm{Lmin^{-1}}$ release rate distribution shows a skew towards higher $\ln([\mathrm{CH_4}]_{\mathrm{area}})$ values (left-skewed), visible by its concave curve in its QQ plot, explaining the rejection of normality by the SW test.

In the Utrecht II dataset, the right skewed distribution of the 0.15 $\mathrm{Lmin^{-1}}$ release could be caused by the peak detection threshold, cutting of part of the distribution. The three releases which fail both tests (15, 80 and 100 $\mathrm{Lmin^{-1}}$) show a bimodal disribution, which appears as s-shape in the QQ plot (Fig. S18).

The London I Day2-70 $\mathrm{Lmin^{-1}}$ release exhibits a left-skewed distribution according to both the histogram and QQ plot (departing in negative direction from the 1:1 line for both margins) and fails both tests (Fig. S19). The QQ plot for the Day3-70 $\mathrm{Lmin^{-1}}$ release suggests normality, similar to the Lilliefors test, only disturbed by two outliers, which could be the reason why the SW test failed.

Similar to the good performance of the distributions of the London II data in the two test statistics, the visual observation of the histogram and QQ plots also shows normality in almost all cases (Fig. S20). The Day2-5.64 $\mathrm{Lmin^{-1}}$ release does not show large deviations in the QQ plot but exhibits an outlier which likely causes the SW test to fail.

Generally, as the release rates increase, a shift of the centre of the distributions towards higher $\ln([\mathrm{CH_4}]_{\mathrm{area}})$ values is observed. For the majority of $\ln([\mathrm{CH_4}]_{\mathrm{area}})$ distributions the QQ plots suggest normality, confirming the evaluation of the test statistics. In some cases, a failed test statistic may be due to the presence of outliers, while the QQ plot for the remaining distribution suggests normality. Notwithstanding, severe departures from normality exist.

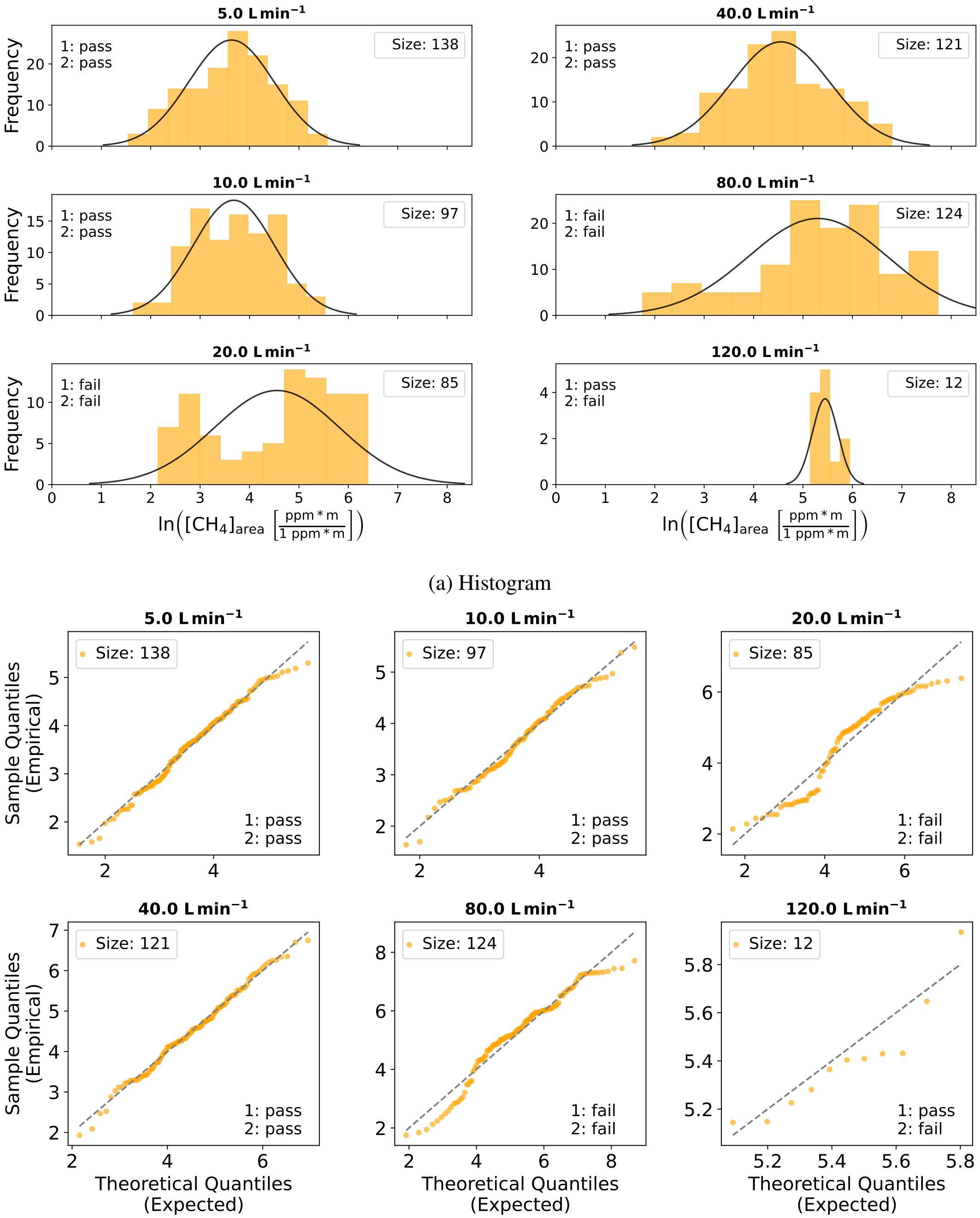

(a) Histogram

(b) Quantile-Quantile plot

Figure S16. Rotterdam: Assessment of log-normality. (a) Histogram of the logarithmically transformed integrated peak area of the measured CH_4 enhancements. Each histogram represents areas measured at a given release rate. A Gaussian distribution is fitted to the data and the results of two normality tests (1: Shapiro-Wilk and 2: Lilliefors) are shown as well as the size of the data set. (b) Quantile-Quantile plot of the logarithmically transformed integrated peak area ($\ln([\mathrm{CH_4}]_{\mathrm{area}})$) versus a normal distribution for each release rate separately.

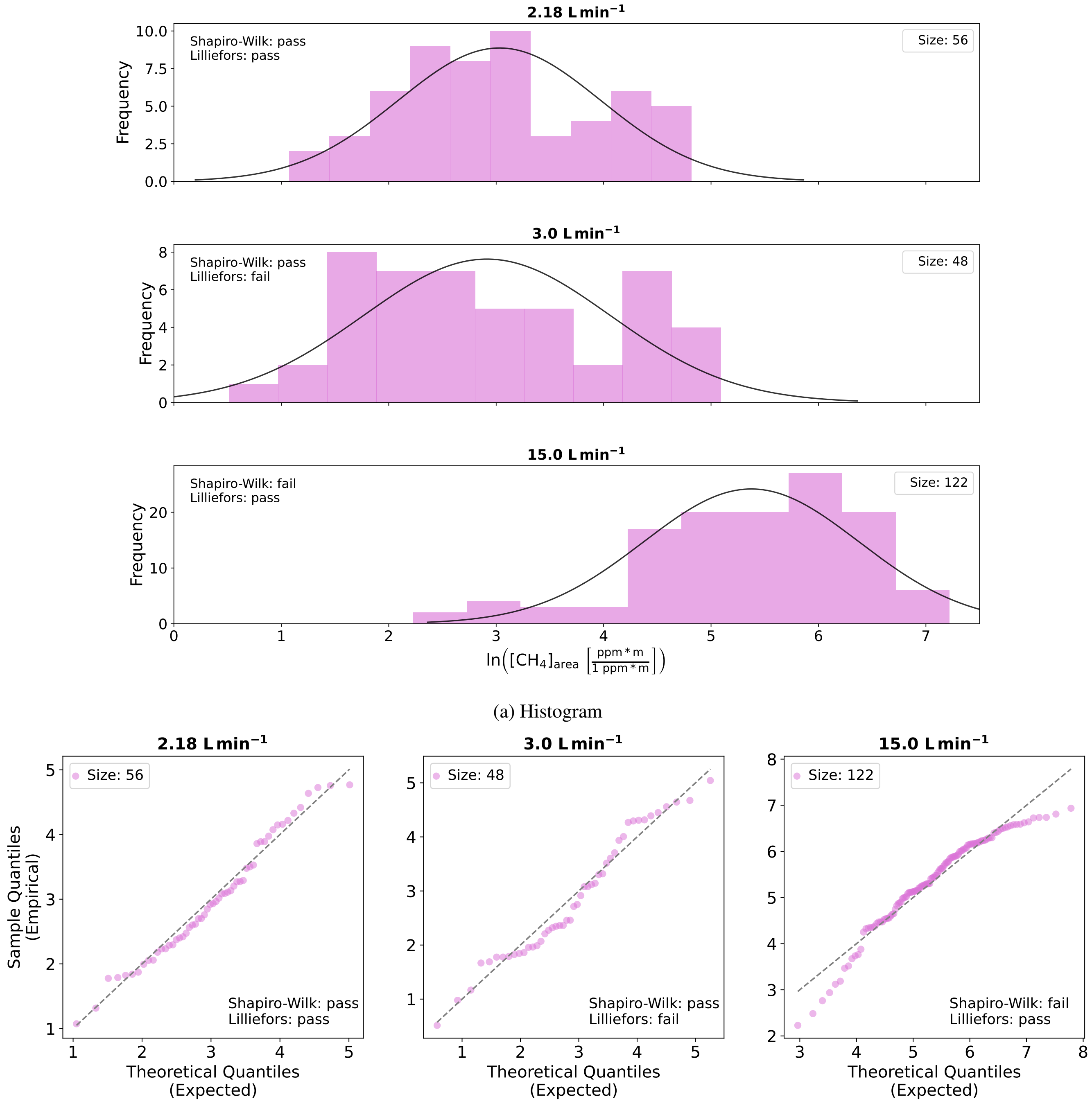

(a) Histogram

(b) Quantile-Quantile plot

Figure S17. Utrecht I: Assessment of log-normality. (a) Histogram of the logarithmically transformed integrated peak area of the measured CH_4 enhancements. Each histogram represents areas measured at a given release rate. A Gaussian distribution is fitted to the data and the results of two normality tests (Shapiro-Wilk and Lilliefors) are shown as well as the size of the data set. (b) Quantile-Quantile plot of the logarithmically transformed integrated peak area ($\ln([\mathrm{CH}_4]_{\mathrm{area}})$) versus a normal distribution for each release rate separately.

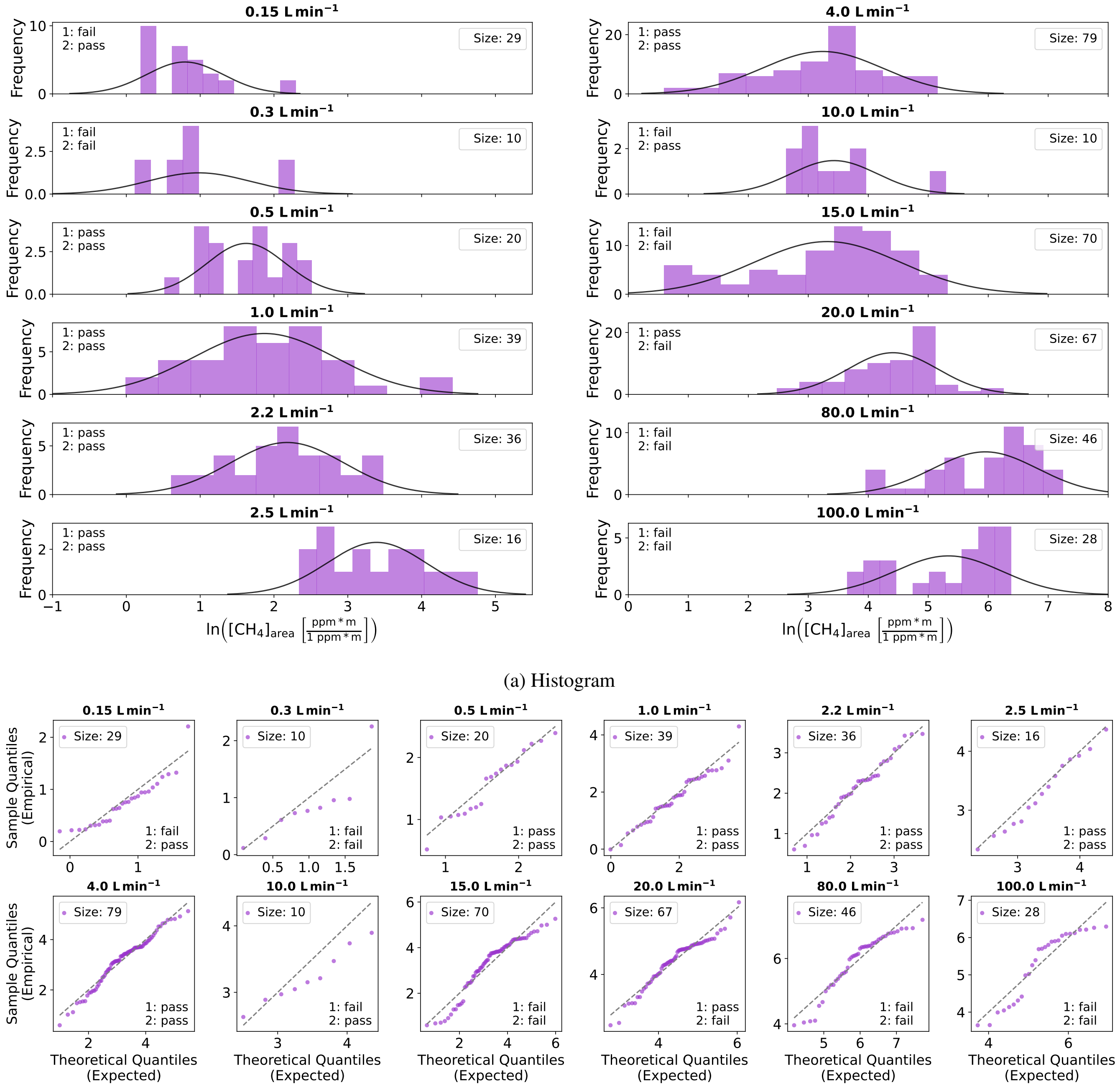

(a) Histogram

(b) Quantile-Quantile plot

Figure S18. Utrecht II: Assessment of log-normality. (a) Histogram of the logarithmically transformed integrated peak area of the measured CH_4 enhancements. Each histogram represents areas measured at a given release rate. A Gaussian distribution is fitted to the data and the results of two normality tests (1: Shapiro-Wilk and 2: Lilliefors) are shown as well as the size of the data set. (b) Quantile-Quantile plot of the logarithmically transformed integrated peak area ($\ln([\mathrm{CH_4}]_{\mathrm{area}})$) versus a normal distribution for each release rate separately.

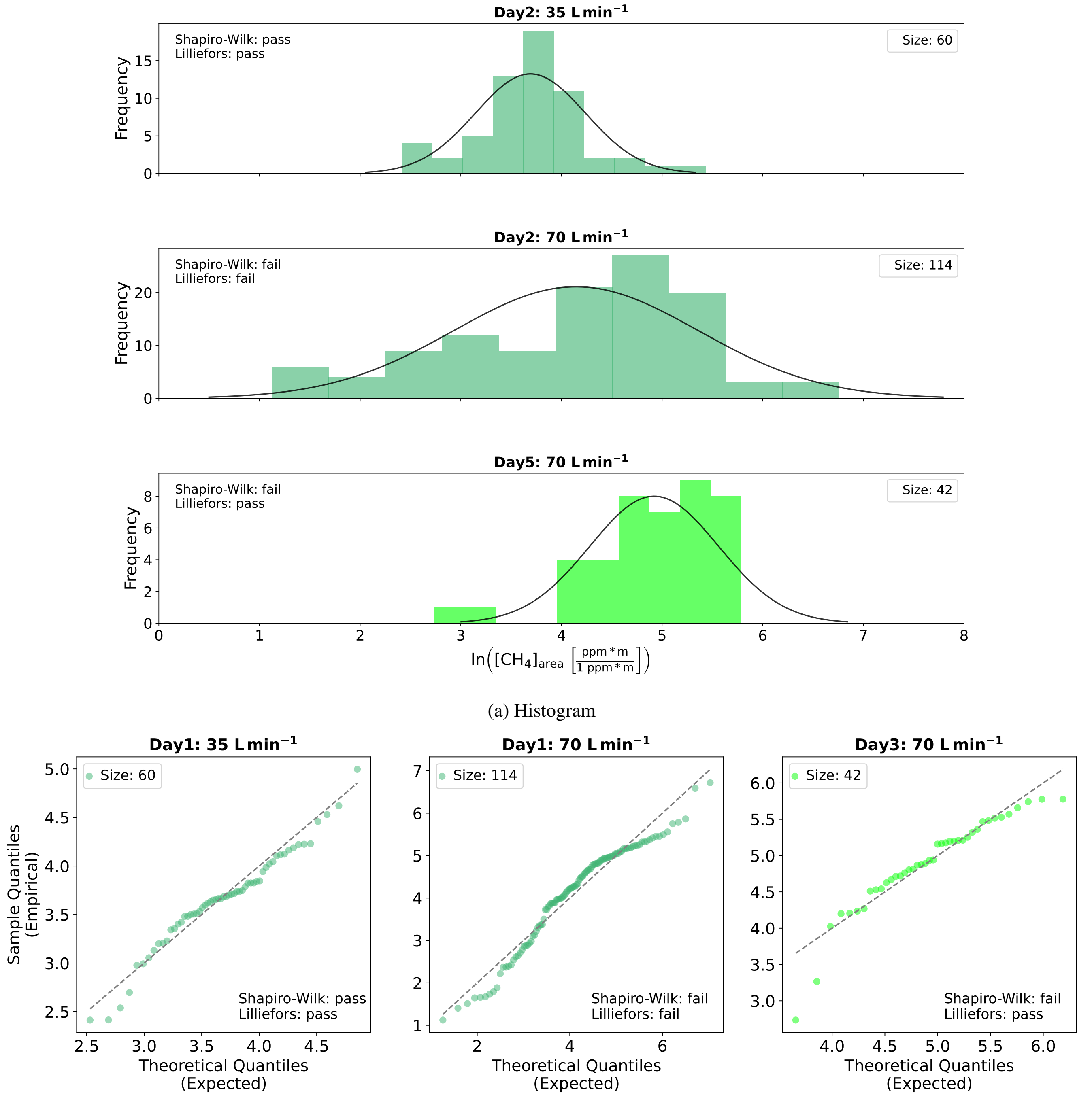

(a) Histogram

(b) Quantile-Quantile plot

Figure S19. London I: Assessment of log-normality. (a) Histogram of the logarithmically transformed integrated peak area of the measured CH_4 enhancements. Each histogram represents areas measured at a given release rate. A Gaussian distribution is fitted to the data and the results of two normality tests (Shapiro-Wilk and Lilliefors) are shown as well as the size of the data set. (b) Quantile-Quantile plot of the logarithmically transformed integrated peak area ($\ln([\mathrm{CH}_4]_{\mathrm{area}})$) versus a normal distribution for each release rate separately.

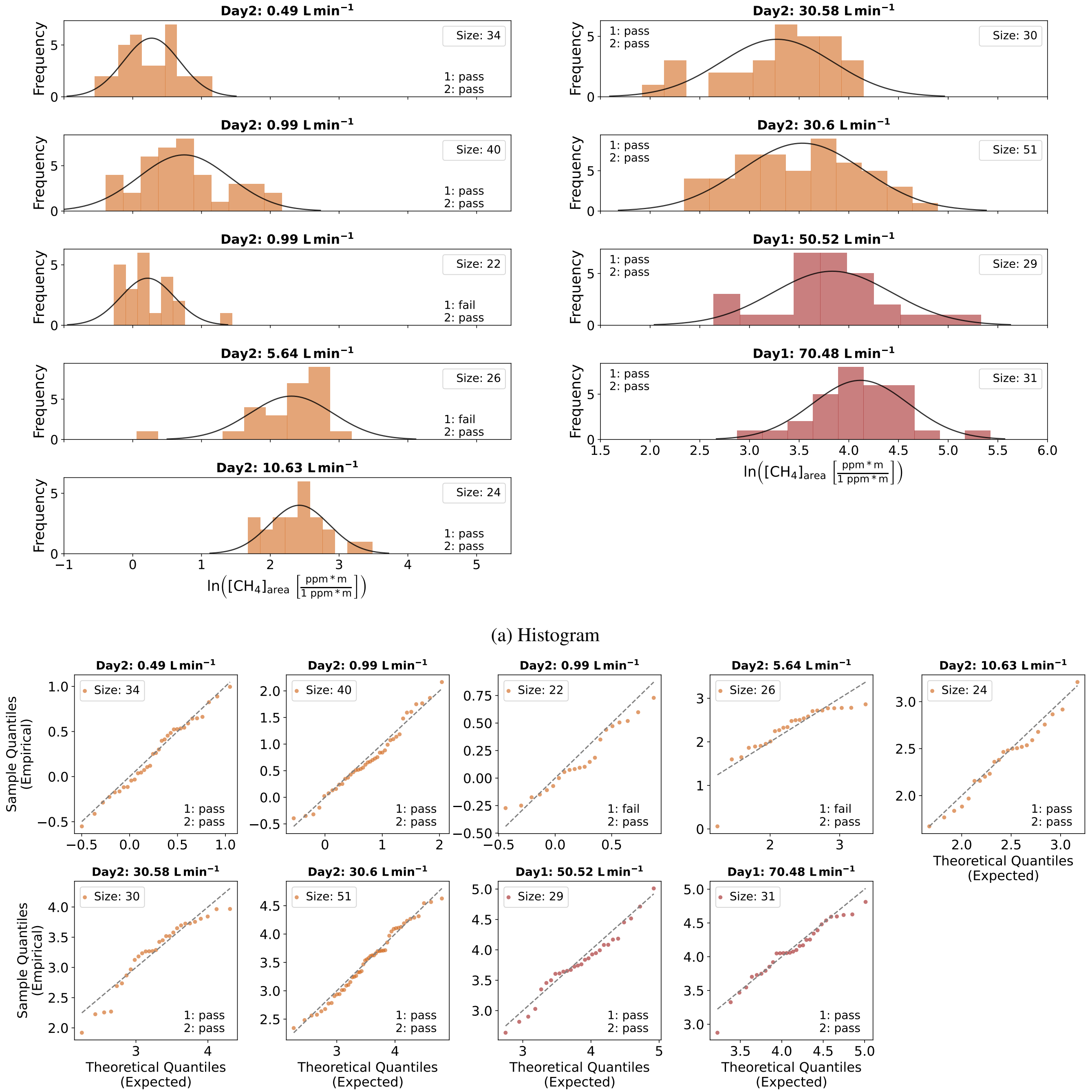

(a) Histogram

(b) Quantile-Quantile plot

Figure S20. London II: Assessment of log-normality. (a) Histogram of the logarithmically transformed integrated peak area of the measured CH_4 enhancements. Each histogram represents areas measured at a given release rate. A Gaussian distribution is fitted to the data and the results of two normality tests (1: Shapiro-Wilk and 2: Lilliefors) are shown as well as the size of the data set. (b) Quantile-Quantile plot of the logarithmically transformed integrated peak area ($\ln([\mathrm{CH}_4]_{\mathrm{area}})$) versus a normal distribution for each release rate separately.

S8 Instrument Performance: Peak Maximum and Spatial Peak Area

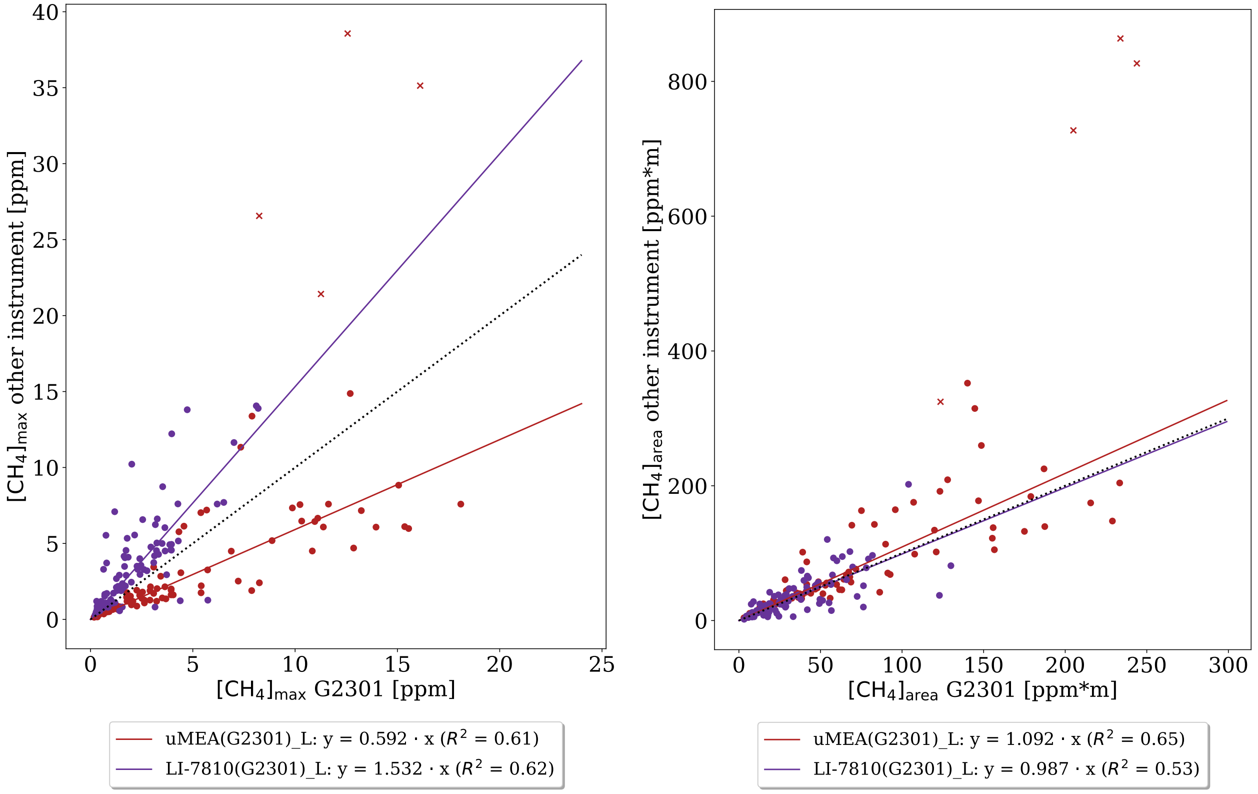

(a) Peak Maximum

(b) Spatial Peak Area

Figure S21. Comparison of peak maximum (a) and spatial peak area (b) from different instruments in London I (Day1 and Day2). Regression fits with intercept 0 are applied to the data for each instrument. The results from the uMEA and LI-7810 analyzers are plotted on the y-axis and the results from the G2301-m instrument on the x-axis. The black dotted line represents the 1:1 line. (Peaks exceeding a maximum of $20\ \mathrm{ppm}$ are marked with an 'x' and were excluded from the fitting process.)

S9 Categorization of Emission Rate per Location

For each peak, the corresponding emission rate was estimated using the empirical function derived from the total dataset as presented in the main manuscript. Subsequently, a category was assigned to each peak, depending on the estimated emission size. In Tab. S8 the four different categories (1-Very low, 2-Low, 3-Medium and 4-High) are defined as well as corresponding maxima and area ranges for the two emission rate estimation methods, e.g. a peak with a spatial peak area of 56 $\mathrm{ppm} * \mathrm{m}$ $(25 < 56 > 109\ \mathrm{ppm} * \mathrm{m})$ will be assigned an emission rate between 6-40 Lmin^{-1} and therefore categorized as a medium leak. As measurements in different locations can exhibit different offsets in their distribution, the categorization performance varies across locations. This is visualized in Fig. S22–Fig. S23. This means that at certain locations, the statistical model may not perform well due to specific characteristics of the built environment. For example, narrow streets with tall buildings can either create tunnelling effects with high wind velocities or block the wind, resulting in very low velocities, depending on their orientation relative to the main wind direction and surrounding structures. Even at the same location, varying weather conditions on different days can influence the plume shape, leading to fluctuations in categorization success rates. For instance, while on Day1 of the London II controlled release experiment over 50% of low-emission-rate peaks were correctly classified, only 20% of peaks in the same emission category were correctly classified the following day.

Table S8. Natural gas distribution network $\mathrm{CH_4}$ emission categories. Corresponding maxima ranges and area ranges are given for the two emission rate estimation methods.

Class	Emission Rate $\left[\mathrm{Lmin}^{-1}\right]$	Weller eq. $[\mathrm{ppm}]$	Area eq. $[\mathrm{ppm} * \mathrm{m}]$
High	> 40	> 7.6	> 109
Medium	$6 - 40$	$1.6 - 7.6$	$25 - 109$
Low	$0.5 - 6$	$0.2 - 1.59$	$3.7 - 25$
Very Low	< 0.5	< 0.2	< 3.7

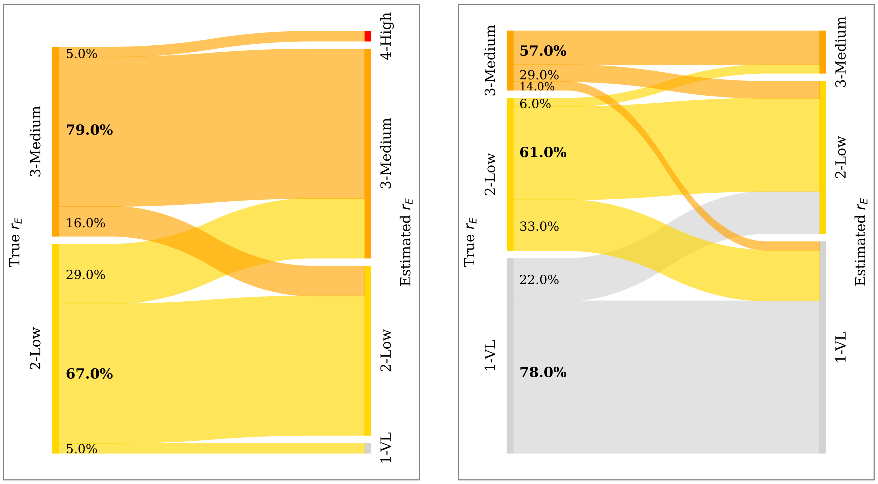

(a) Toronto Day1

(b) Toronto Day2

Figure S22. Categorization performance for data obtained in Toronto. The left y axis represents the true emission rate r_E, where the width of the bars indicate the amount of plumes belonging to each emission category (categories: 1-Very Low, 2-Low, 3-Medium and 4-High). The right y axis represents the categories estimated by the statistical model and the connecting lines visualize the amount of plumes from each category pool which the algorithm classifies into another (or the same) category.

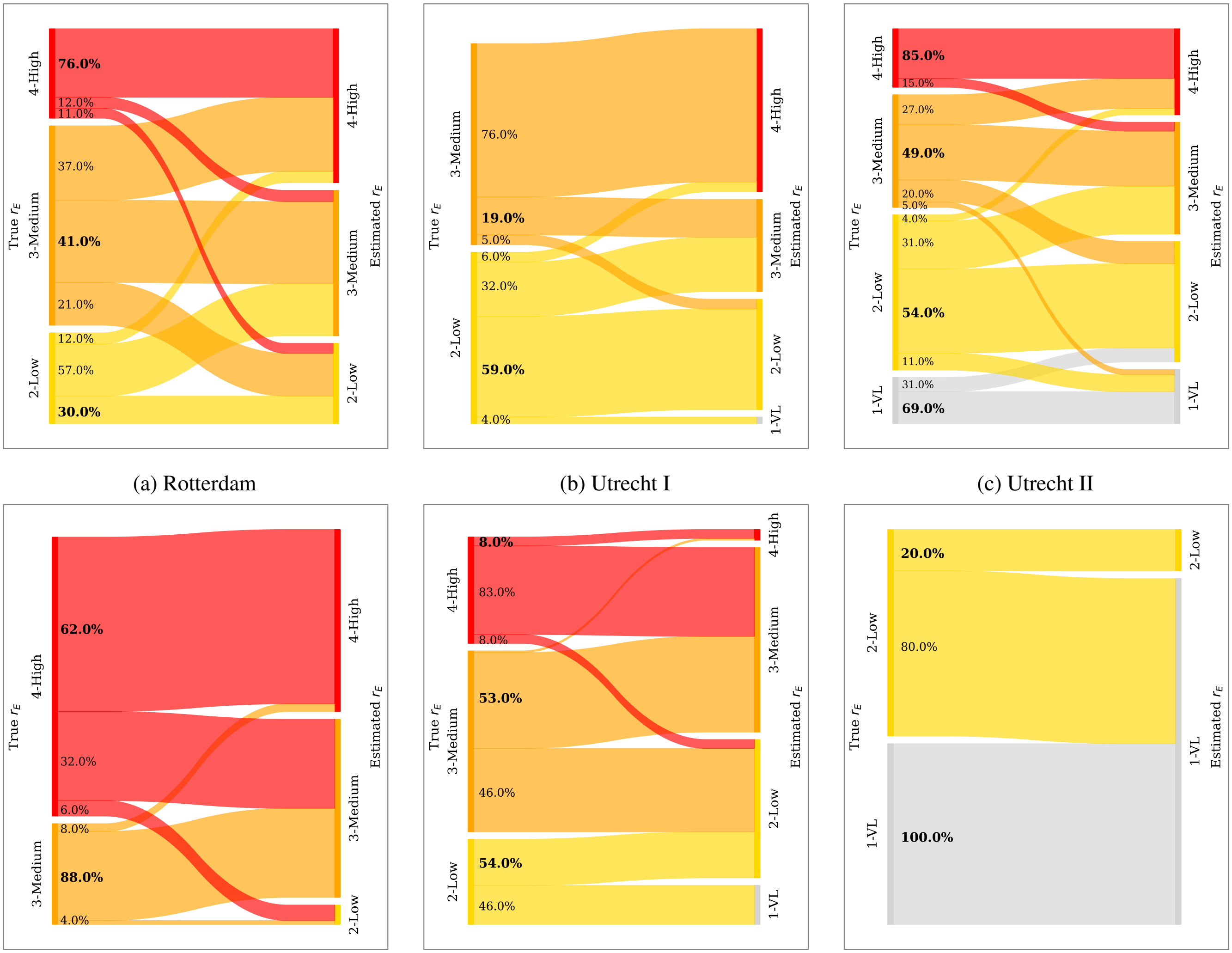

(a) Rotterdam

(b) Utrecht I

(c) Utrecht II

(d) London I

(e) London II Day1

(f) London II Day2

Figure S23. Categorization performance for data obtained in Rotterdam, Utrecht I, Utrecht II, London I and London II. The left y axis represents the true emission rate r_E, where the width of the bars indicate the amount of plumes belonging to each emission category (categories: 1-Very Low, 2-Low, 3-Medium and 4-High). The right y axis represents the categories estimated by the statistical model and the connecting lines visualize the amount of plumes from each category pool which the algorithm classifies into another (or the same) category.

S10 Influence of Sampling Effort

S10.1 Hypothetical Distributions

In order to illustrate the behaviour of sampling multiple times at the same locations, we present results for some selected hypothetical distributions with means falling above or below the empirical equation derived from the totality of all measurements in the main manuscript. Fig. S24 and Fig. S25 display hypothetical distributions randomly sampled with standard deviations of 1 and different offsets for the release rates 3 Lmin^{-1} and 50 Lmin^{-1}. A 'perfect' distribution is included for which the mean corresponds to the $\ln([\mathrm{CH}_4]_{\mathrm{area}})$ value that we expect for this release rate following the Area eq. The offsets are selected so that, in log space, they maintain an equal distance from the mean of the ideal distribution in both positive and negative directions (e.g., ± 0.7 for the distributions with a small positive and small negative offsets).

For the 3 Lmin^{-1} case, the percentage difference of the estimated release rates to the calculated mean emission rate decreases to 0 as expected (Fig. S24b). The absolute percentage error decreases for a higher number of transects for all distributions except for the ones with a large negative offset. The percentage error is greater for the distribution with a small positive offset compared to that with a small negative offset. The distribution with the large positive offset shows the highest percentage error relative to the true emission rate. Interestingly, however, it has the smallest percentage error when compared to the calculated mean emission rate.

For the 50 Lmin^{-1} case, the percentage difference of the estimated release rates to the calculated mean emission rate decreases to 0 as expected, except for the distribution with the high positive offset (Fig. S25b). This is due to the fact that the mean of the distribution corresponds to a release rate higher then the cap of 200 Lmin^{-1}. The absolute percentage error decreases only for the perfect distribution and the ones with a small negative or positive offset.

The two example shows that generally the error in estimations decreases when including more transects. However, in case of a large deviation of the measurement distribution from the one we expect following our method the behaviour can differ. Apart from the offset itself, other parameters play a role such as the imposed emission rate cap and likely the standard deviation or presence of outlier.

Fig. S26 and Fig. S27 illustrate the calculations steps from the $\ln([\mathrm{CH}_4]_{\mathrm{area}})$ distribution to the final mean absolute percentage differences. In panel (a), the underlying distribution is shown in gray, with black markers representing the means of different Monte Carlo samples of size N. As sample size increases, the spread of the sample means narrows until it converges to the overall distribution mean at $N = 60$, the population size. Panel (b) depicts the emission rate estimates derived from the sample means in (a). As sample size grows, variability in the emission rate estimates diminishes. Further, it is evident that larger overestimations than underestimations occur. Panel (c) presents the percentage deviations of the estimated emission rate from the true rate, showing both positive and negative directions. Finally, panel (d) displays the absolute percentage deviations, similar to Figure 5 in the main manuscript.

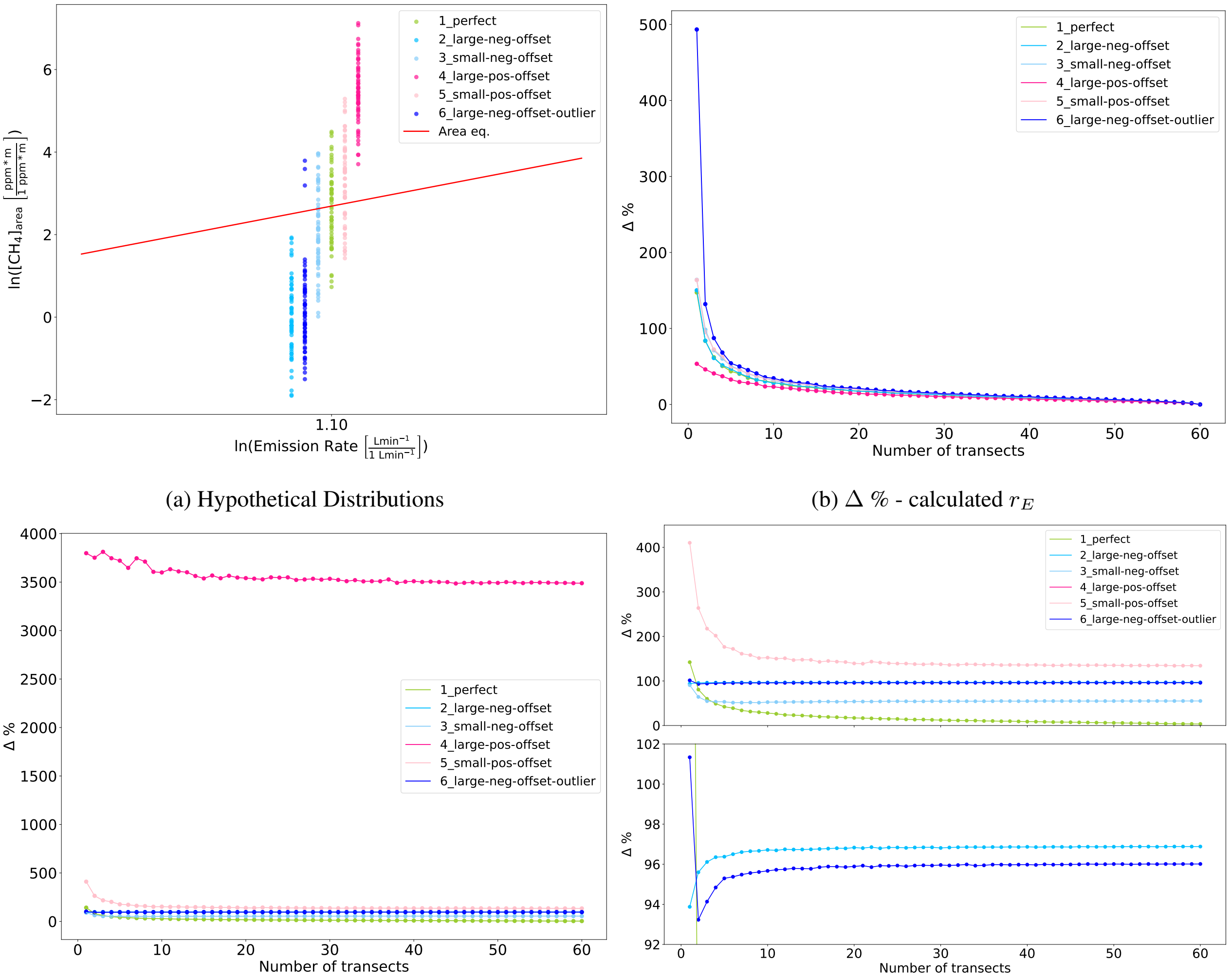

(a) Hypothetical Distributions

(b) Δ % - calculated r_E

(c) Δ % - true r_E

(d) Δ % - true r_E Zoom

Figure S24. Hypothetical distributions for a release rate 3 Lmin^{-1} with different offsets from the perfect distribution.

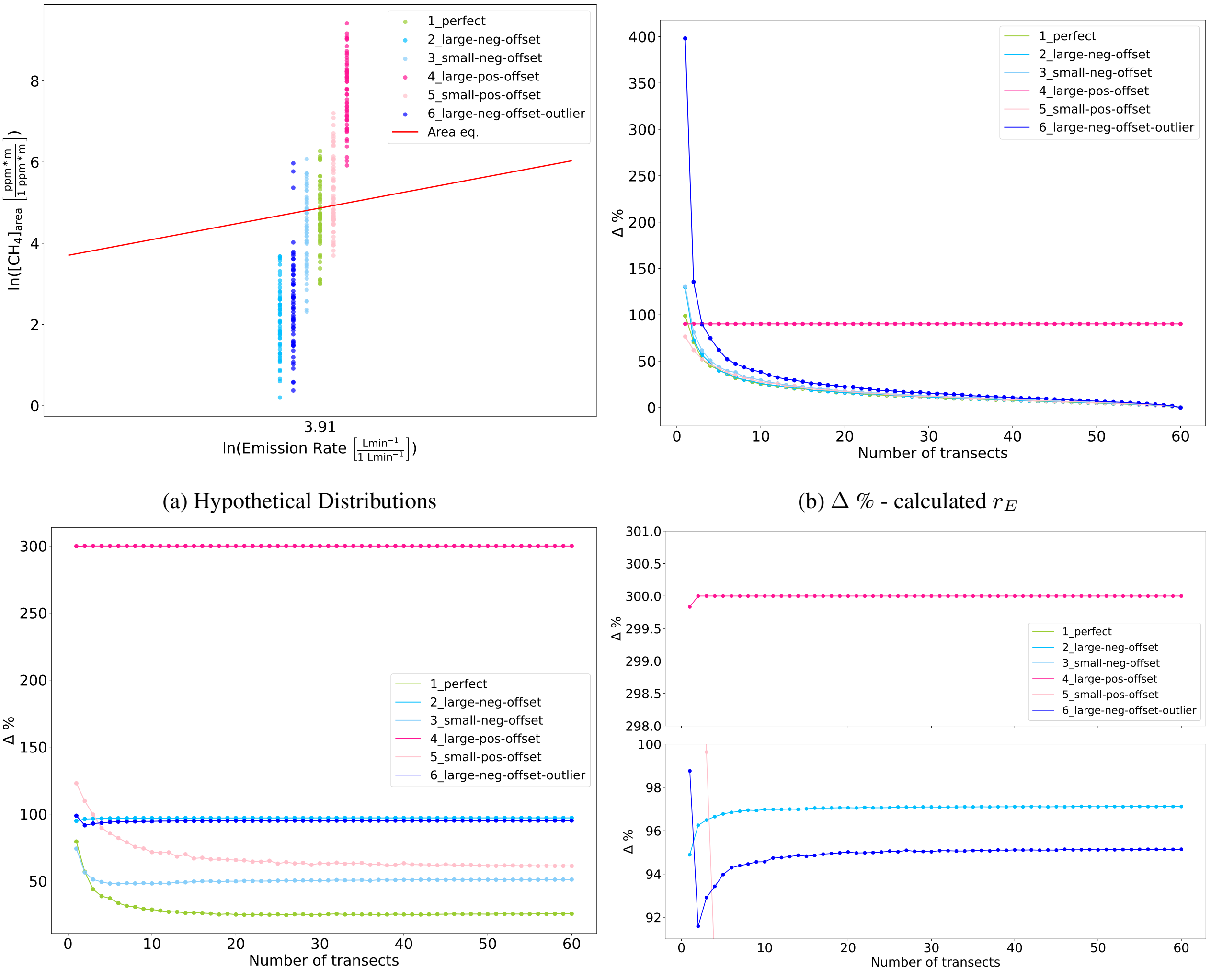

(a) Hypothetical Distributions

(b) Δ % - calculated r_E

(c) Δ % - true r_E

(d) Δ % - true r_E Zoom

Figure S25. Hypothetical distributions for a release rate 50 Lmin^{-1} with different offsets from the perfect distribution.

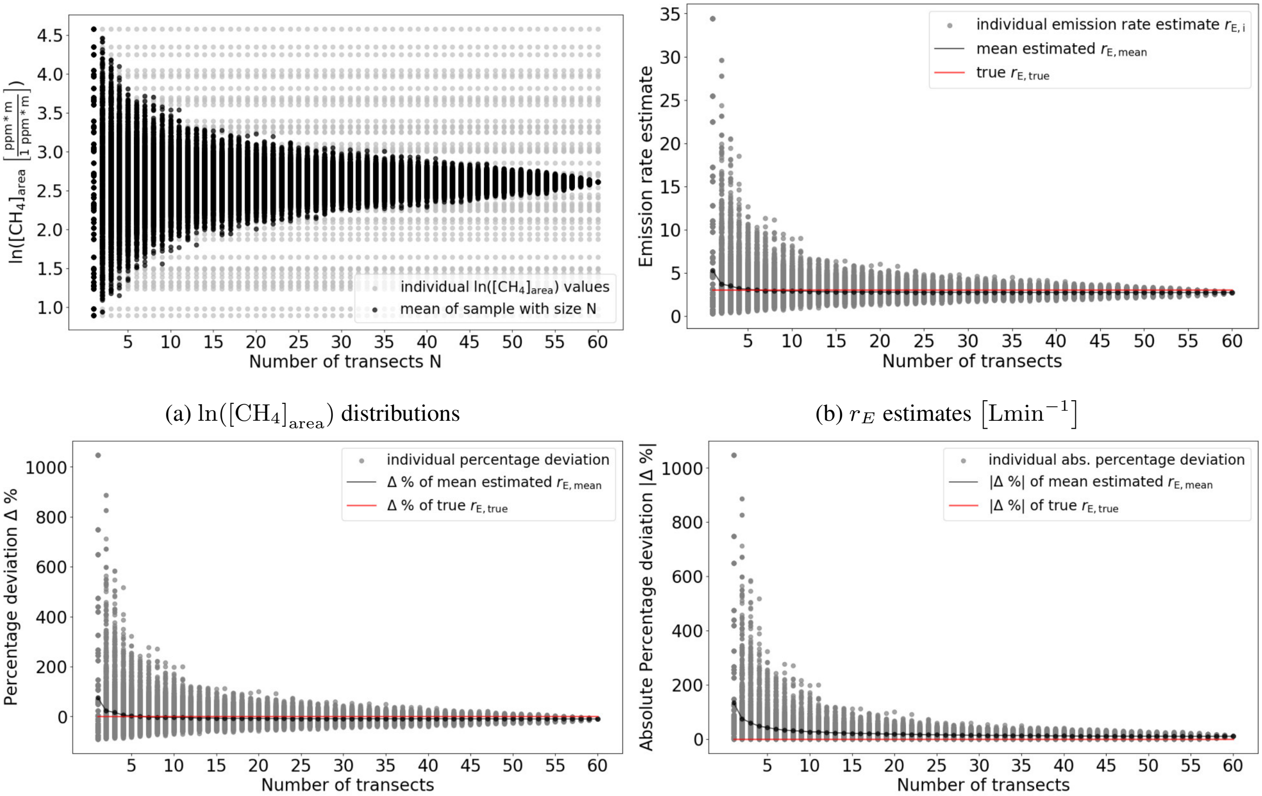

(a) $\ln([\mathrm{CH}_4]_{\mathrm{area}})$ distributions

(b) r_E estimates $\left[\mathrm{Lmin}^{-1}\right]$

(c) Δ % - r_E from true r_E

(d) Absolute Δ % - r_E from true r_E

Figure S26. Perfect distribution: Visualization of different calculation steps in the analysis of the benefit of multiple transects.

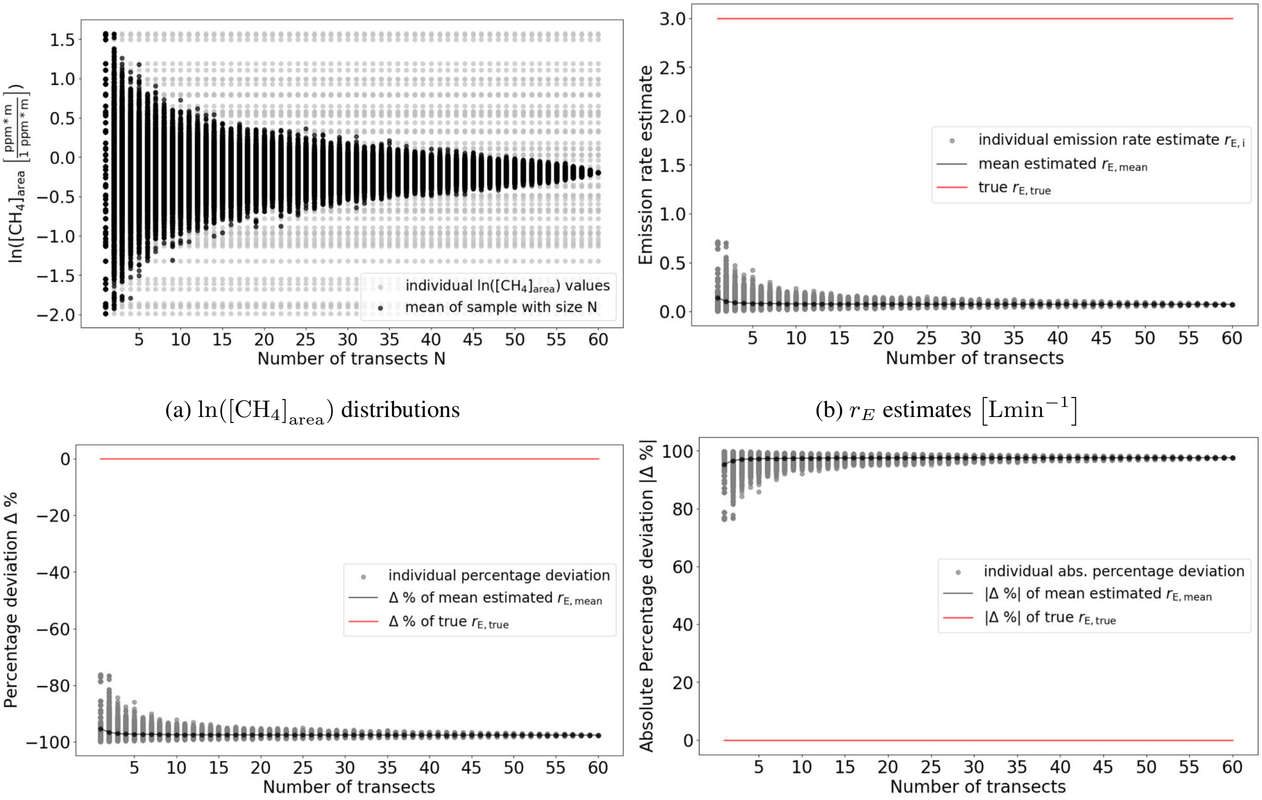

(a) $\ln([\mathrm{CH_4}]_{\mathrm{area}})$ distributions

(b) r_E estimates $[\mathrm{Lmin^{-1}}]$

(c) Δ % - r_E from true r_E

(d) Absolute Δ % - r_E from true r_E

Figure S27. Distribution with large negative offset: Visualization of different calculation steps in the analysis of the benefit of multiple transects.

Code and data availability. The python code and a sub-sample of the data used to produce the results in this article are available on GitHub: https://github.com/judith-tettenborn/CRE_CH4Quantification.git

References

Ars, S., Vogel, F., Arrowsmith, C., Heerah, S., Knuckey, E., Lavoie, J., Lee, C., Pak, N. M., Phillips, J. L., and Wunch, D.: Investigation of the Spatial Distribution of Methane Sources in the Greater Toronto Area Using Mobile Gas Monitoring Systems, Environmental Science & Technology, 54, 15 671–15 679, https://doi.org/10.1021/acs.est.0c05386, 2020.

Biecek, P. and Burzykowski, T.: Explanatory Model Analysis: Explore, Explain, and Examine Predictive Models, CRC Press, New York, ISBN 978-0-367-13559-1, https://www.taylorfrancis.com/books/mono/10.1201/9780429027192/explanatory-model-analysis-przemyslaw-biecek-tomasz-burzykowski, 2021.

Flatt, C. and Jacobs, R. L.: Principle Assumptions of Regression Analysis: Testing, Techniques, and Statistical Reporting of Imperfect Data Sets, Advances in Developing Human Resources, 21, 484–502, https://doi.org/10.1177/1523422319869915, 2019.

Keskin, S.: Comparison of Several Univariate Normality Tests Regarding Type I Error Rate and Power of the Test in Simulation Based Small Samples, Journal of Applied Science Research, 2, 296–300, https://www.academia.edu/download/88717042/296-300.pdf, 2006.

Nimon, K.: Statistical Assumptions of Substantive Analyses Across the General Linear Model: A Mini-Review, Frontiers in Psychology, 3, https://doi.org/10.3389/fpsyg.2012.00322, 2012.

Razali, N. M. and Wah, Y. B.: Power Comparisons of Shapiro-Wilk, Kolmogorov-Smirnov, Lilliefors and Anderson-Darling Tests, Journal of Statistical Modeling and Analytics, 2, 21–33, 978-967-363-157-5, 2011.

von Fischer, J. C., Cooley, D., Chamberlain, S., Gaylord, A., Griebenow, C. J., Hamburg, S. P., Salo, J., Schumacher, R., Theobald, D., and Ham, J.: Rapid, Vehicle-Based Identification of Location and Magnitude of Urban Natural Gas Pipeline Leaks, Environmental Science & Technology, 51, 4091–4099, https://doi.org/10.1021/acs.est.6b06095, 2017.

Von Storch, H. and Zwiers, F. W.: Statistical Analysis in Climate Research, Cambridge University Press, ISBN 978-1-139-42509-4, 2002.

Weller, Z. D., Roscioli, J. R., Daube, W. C., Lamb, B. K., Ferrara, T. W., Brewer, P. E., and von Fischer, J. C.: Vehicle-Based Methane Surveys for Finding Natural Gas Leaks and Estimating Their Size: Validation and Uncertainty, Environmental Science & Technology, 52, 11 922–11 930, https://doi.org/10.1021/acs.est.8b03135, 2018.